



January 11–14, 2015 • Doha, Qatar

CONGRESS PROCEEDINGS



EDITORS:
Ibrahim Karaman
Raymundo Arróyave
Eyad Masad

TMS

WILEY



**TMS Middle East - Mediterranean Materials Congress
on Energy and Infrastructure Systems (MEMA 2015)**

January 11–14, 2015 • Doha, Qatar

CONGRESS PROCEEDINGS

LAUNCH THE PROCEEDINGS

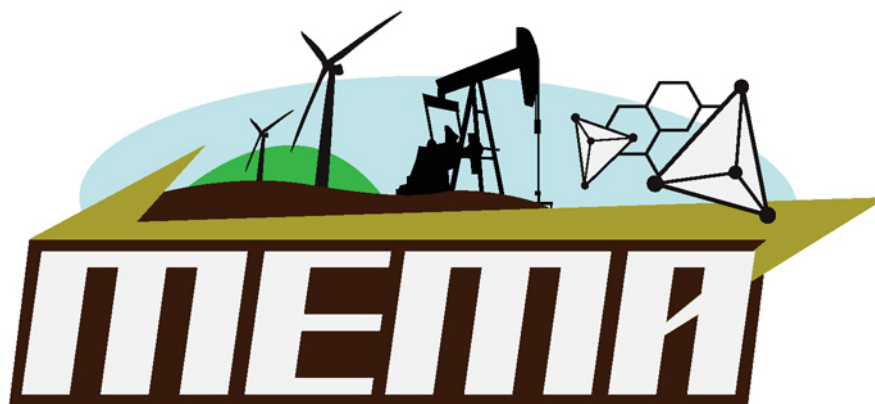
SEARCH

ABOUT TMS

CD HELP

WILEY

TMS



**Proceedings of the
TMS Middle East - Mediterranean Materials
Congress on Energy and Infrastructure
Systems (MEMA 2015)**

Held

January 11–14, 2015

Doha, Qatar

Edited by

Ibrahim Karaman

Raymundo Arróyave

Eyad Masad

WILEY

TMS

**Copyright © 2015 by The Minerals, Metals & Materials Society.
All rights reserved.**

**Published by John Wiley & Sons, Inc., Hoboken, New Jersey.
Published simultaneously in Canada.**

No part of this publication may be reproduced, stored in a retrieval system, or transmitted in any form or by any means, electronic, mechanical, photocopying, recording, scanning, or otherwise, except as permitted under Section 107 or 108 of the 1976 United States Copyright Act, without either the prior written permission of The Minerals, Metals, & Materials Society, or authorization through payment of the appropriate per-copy fee to the Copyright Clearance Center, Inc., 222 Rosewood Drive, Danvers, MA 01923, (978) 750-8400, fax (978) 750-4470, or on the web at www.copyright.com. Requests to the Publisher for permission should be addressed to the Permissions Department, John Wiley & Sons, Inc., 111 River Street, Hoboken, NJ 07030, (201) 748-6011, fax (201) 748-6008, or online at <http://www.wiley.com/go/permission>.

Limit of Liability/Disclaimer of Warranty: While the publisher and author have used their best efforts in preparing this book, they make no representations or warranties with respect to the accuracy or completeness of the contents of this book and specifically disclaim any implied warranties of merchantability or fitness for a particular purpose. No warranty may be created or extended by sales representatives or written sales materials. The advice and strategies contained herein may not be suitable for your situation. You should consult with a professional where appropriate. Neither the publisher nor author shall be liable for any loss of profit or any other commercial damages, including but not limited to special, incidental, consequential, or other damages.

Wiley also publishes books in a variety of electronic formats. Some content that appears in print may not be available in electronic formats. For more information about Wiley products, visit the web site at www.wiley.com. For general information on other Wiley products and services or for technical support, please contact the Wiley Customer Care Department within the United States at (800) 762-2974, outside the United States at (317) 572-3993 or fax (317) 572-4002.

Library of Congress Cataloging-in-Publication Data is available.

ISBN 978-1-119-06527-2

Printed in the United States of America.

10 9 8 7 6 5 4 3 2 1

WILEY

TMS

TABLE OF CONTENTS

TMS Middle East - Mediterranean Materials Congress on Energy and Infrastructure Systems (MEMA 2015)

Preface	ix
Editors/Organizers	xi
Acknowledgments	xiii
MEMA Organizers	xv

Sustainable Infrastructure Materials

Corrosion Challenges for the Oil and Gas Industry in the State of Qatar	3
<i>R. Johnsen</i>	
Utilising Fine and Coarse Recycled Aggregates from the Gulf Region in Concrete	13
<i>M. Jones, J. Halliday, L. Csetenyi, L. Zheng, and N. Strompinis</i>	
Finite Element Simulation of the Response of No-Tension Materials.....	25
<i>A. Alipour and T. Scarpas</i>	
Investigation and Modeling of the Fatigue Damage in Natural Fiber Composites	35
<i>H. Bougherara, I. Sawi, Z. Fawaz, and F. Meraghni</i>	
Improving Asphalt Mixtures Performance by Mitigating Oxidation Using Anti-Oxidants Additives	45
<i>S. Dessouky and M. Diaz</i>	
Effect of Warm Mix Asphalt on Aging of Asphalt Binders	55
<i>A. Abbas, M. Nazzal, S. Kaya, S. Akinbowale, B. Subedi, and L. Qtaish</i>	
An Innovative Concept for Testing Rutting Susceptibility of Asphalt Mixture	65
<i>A. Mohseni and H. Azari</i>	
Evaluation of Asphalt Mixes Workability and Compactability Using Laboratory and Accelerated Field Testing	77
<i>S. Dessouky and M. Diaz</i>	
Effect of Electroless Ni-Co-P and Co-P Coatings on Cavitation Erosion Resistance	87
<i>S. Karrab, M. Aboraia, M. Doheim, and S. Ahmed</i>	
Influence of Joining Time on Microstructure and Mechanical Properties of TLP-Joined IN-738LC to GTD-111.....	99
<i>M. Ghadi, M. Amjadi, M. Shahriari, and M. Ghomi</i>	
Direct Observation of Effects of Foam Density, Gating Design and Pouring Temperature on Mold Filling Process in Lost Foam Casting of A356 Alloy.....	109
<i>A. Sharifi, M. Abadi, and R. Ashiri</i>	
Control of Grain Refinement of A356 Aluminum Alloy by Computer Aided Cooling Curve Analysis	119
<i>A. Sharifi and N. Arab</i>	

Pulsed Electrodeposition of Ni with Uniform Co-Deposition of Micron Sized Diamond Particles on Copper Substrate.....	129
<i>P. Kumar and N. Mahato</i>	

Materials for Energy Extraction and Storage: Shape Memory Alloys

The Turnable Microstructure and Its Influence on the Giant Magnetocaloric Effect in Magnetic Shape Memory Alloys.....	139
<i>N. Bruno, I. Karaman, J. Ross, Y. Huang, and J. Li</i>	
Studies of Magnetic Properties of Ni-Mn-In-Co Heusler-Type Glass-Coated Microwires.....	149
<i>V. Zhukova, M. Ipatov, A. Aronin, G. Abrosimova, A. Kiselev, and A. Zhukov</i>	
Optimization of Soft Magnetic Properties in Nanocrystalline Glass-Coated Microwires.....	157
<i>V. Zhukova, A. Talaat, M. Ipatov, J. Val, J. Blanco, L. Gonzalez-Legarreta, B. Hernando, and A. Zhukov</i>	
On the Fracture Response of Shape Memory Alloy Actuators.....	165
<i>S. Jape, A. Parrinello, T. Baxevanis, and D. Lagoudas</i>	
Development of SMA Actuated Morphing Airfoil for Wind Turbine Load Alleviation.....	181
<i>A. Karakalas, T. Machairas, A. Solomou, V. Riziotis, and D. Saravanos</i>	
Identification of Model Parameter for the Simulation of SMA Structures Using Full Field Measurements.....	191
<i>Y. Chemisky, F. Meraghni, N. Bourgeois, S. Cornell, R. Echchorfi, and E. Patoor</i>	
Comparison of the Work Output Values of Gradually Changing Porosity Samples and the Samples with Single Percent Porosity Level.....	201
<i>H. Tugrul, S. Cakmak, and B. Kockar</i>	
Phenomenological Model for Phase Transformation Characteristics of Textured Shape Memory Alloys.....	211
<i>D. Chatziathanasiou, Y. Chemisky, F. Meraghni, G. Chatzigeorgiou, and E. Patoor</i>	

Lightweight and High Performance Materials

Microstructural Design of Mg Alloys for Lightweight Structural Applications.....	225
<i>E. Dogan, M. Vaughan, I. Karaman, G. Proust, G. Ayoub, and A. Benzerga</i>	
The Effect of Tool Geometry on Material Mixing during Friction Stir Welding (FSW) of Magnesium AZ31B Welds.....	235
<i>Z. Chlouk, H. Achdjian, G. Ayoub, G. Kridli, and R. Hamade</i>	
Damage Mechanisms at Various Strain Rates and Temperatures in AZ31B Magnesium Alloy.....	243
<i>A. Rodriguez, G. Ayoub, and A. Benzerga</i>	
Hybrid Aluminum and Natural Fiber Composite Structure for Crash Safety Improvement.....	249
<i>S. Helaili, M. Chafra, and Y. Chevalier</i>	
Mechanical Response and Evolution of Damage of Al6061-T6 under Different Strain Rates and Temperatures.....	259
<i>A. Dorbane, G. Ayoub, B. Mansoor, R. Hamade, G. Kridli, and A. Imad</i>	
Adhesion Improvement between Polyethylene and Aluminum Using Eco-Friendly Plasma Treatment.....	267
<i>A. Popelka, I. Krupa, I. Novák, M. Ouederni, F. Abdulaqder, S. Al-Yazedi, T. Al-Gunaid, and T. Al-Senani</i>	

Effect of Re Elements on the Sorption Properties of Nanocrystalline Zr-Co Getters Prepared by Mechanical Alloying.....	273
<i>A. Moghadam, V. Dashtizad, A. Kafrou, and H. Yoozbashizadeh</i>	
Principles of Improvement the Energy Efficiency in Pyrometallurgy of Copper: Utilization the Secondary Heat Energy of Intermediate Products.....	283
<i>M. Ćirković, M. Bugarin, V. Trujić, and Ž. Kamberović</i>	

Materials for Energy Conversion and Storage

Numerical Modeling of Cathode Contact Material Densification.....	295
<i>M. Khaleel, B. Koepfel, and E. Stephens</i>	
Perovskites of Type LaBO ₃ Prepared by the Microwave-Assisted Method for Oxygen Production.....	307
<i>S. Ali, N. Atta, Y. Al-Rahman, and A. Galal</i>	
Electrochemical Deposition of High Purity Silicon from Molten Salts.....	319
<i>G. Haarberg</i>	
Cationic (V, Y)-codoped TiO ₂ with Enhanced Visible Light Induced Photocatalytic Activity for Photoelectrochemical Applications.....	325
<i>M. Khan, W. Cao, and B. Mansoor</i>	
Numerical Optimization of Lead Free Perovskite Solar Cell.....	335
<i>M. Hossain, O. Daif, N. Amin, F. Alharbi, and N. Tabet</i>	
Computational Assessment of the Performance of Lead Halide Perovskite Solar Cells Using Inorganic Layers as Hole Transport Materials.....	339
<i>M. Hossain, F. Alharbi, and N. Tabet</i>	
Electrode Materials Based on Phosphates for Lithium Ion Batteries as an Efficient Energy Storage System.....	343
<i>I. Saadoune, K. Lasri, I. Bezza, S. Indris, D. Brandell, and H. Ehrenberg</i>	
Interfacial Stresses and Degradation of Oxide Scale and Substrate Interface at High Temperature.....	351
<i>M. Khaleel, E. Stephens, and J. Stevenson</i>	
Nanomaterials-Based Ultracapacitor for Power Integrated Circuits.....	357
<i>W. Gill and D. Choi</i>	
A Multi-Scale Based Model for Composite Materials with Embedded PZT Filaments for Energy Harvesting.....	361
<i>A. El-Etriby, M. Abdel-Meguid, K. Shalan, T. Hatem, and Y. Bahei-El-Din</i>	
Methane Production from Carbon Dioxide and Increasing Energy Return of Investment (EROI) in Shale Oil.....	381
<i>O. Akoubeh</i>	
Storage and Release of Thermal Energy of Phase Change Materials Based on Linear Low Density of Polyethylene, Parafin Wax and Expanded Graphite Applicable in Building Industry.....	395
<i>P. Sobolciak, M. Karkri, I. Krupa, and M. Maadeed</i>	

Computational Materials Design

Calculation of Electronic Structure and Field Induced Magnetic Collapse in Ferroic Materials.....	405
<i>P. Entel, R. Arróyave, N. Singh, V. Sokolovskiy, and V. Buchelnikov</i>	
Strong Stacking between Organic and Organometallic Molecules as the Key for Material Design.....	409
<i>S. Zarić, D. Malenov, and D. Ninković</i>	
A Biomimetic-Computational Approach to Optimizing the Quantum Efficiency of Photovoltaics.....	415
<i>L. Perez and A. Holzenburg</i>	
Stability and Mechanical Properties of $\{A_xA'_{(1-x)}\}\{B_\gamma B'_{(1-\gamma)}\}O_3$ Ceramics.....	423
<i>B. Akgenc, Ç. Tasseven, and T. Çağın</i>	
Tailoring Thermal Conductivity of Ge/Si Core-Shell Nanowires.....	433
<i>S. Sarikurt, C. Sevik, A. Kinaci, J. Haskins, and T. Cagin</i>	
Thermal Analysis of Solar Panels.....	441
<i>N. Barth, J. Correia, S. Ahzi, and M. Khaleel</i>	
Micromechanical Fatigue Visco-Damage Model for Short Glass Fiber Reinforced Polyamide-66.....	451
<i>N. Despringre, Y. Chemisky, G. Robert, and F. Meraghni</i>	
Alloy Design Strategies through Computational Thermodynamics and Kinetics Approaches.....	461
<i>R. Arróyave, S. Li, R. Zhu, and I. Karaman</i>	
C-Axis Compression of Magnesium Single Crystals: Multi-Scale Dislocation Dynamics Analyses.....	471
<i>W. Jaber and M. Shehadeh</i>	
Multiscale Modeling of Discontinuous Precipitation in U-Nb.....	481
<i>T. Duong and R. Arróyave</i>	
Thermo-Mechanical Description of AISI4140 Steel at Elevated Temperatures.....	491
<i>F. Abed, C. ElSayegh, and A. Abdul-Latif</i>	
Analysis of Thermo-Mechanical Rigidity of Continuously Cast Steel Slabs.....	501
<i>M. El-Bealy</i>	
Simulation of Solidification, Relaxation and Long-Term Behavior of a Borosilicate Glass.....	511
<i>N. Barth, D. George, S. Ahzi, Y. Rémond, M. Khaleel, and F. Bouyer</i>	
A Durability Analysis of Super-Quiet Pavement Structures.....	521
<i>S. Srirangam, K. Anupam, T. Scarpas, C. Kasbergen, and P. The</i>	
Predictive Modeling for Sustainable Energy Solutions.....	531
<i>C. Amrani and O. Bouhali</i>	
Author Index.....	539
Subject Index.....	541

PREFACE

This is a collection of manuscripts presented at The Middle East - Mediterranean Materials Congress on Energy and Infrastructure Systems (MEMA 2015), a specialty conference organized by The Minerals, Metals & Materials Society (TMS) and other institutions. The congress was held in Doha, Qatar on January 11-14, 2015.

The intent of this event was to focus on new materials research and development in applications of interest for Qatar and the entire Middle East and Mediterranean region. The main goal was to build synergy among researchers working on different materials applications but with similar objectives of enhancing design, sustainability, and functionality of materials. The congress was a forum for establishing collaboration among academia, research institutions, and industry in the region and the rest of the world, with a goal to help bring sustainability and stability to the region. Attendees represented government organizations, academic institutions, and industry working in various fields of materials for energy extraction, conversion, and storage; sustainability; as well as cross-cutting approaches in computational materials science. The long-term goal of this materials congress in the region is to further develop it into a periodic international materials congress in the Middle East and Mediterranean.

Over 200 authors and attendees from all over the world contributed to this congress in the form of presentations, lively discussions, and manuscripts presented in this volume. The international advisory committee members representing 9 different countries actively participated and promoted the congress.

The specific tracks and topics highlighted during this congress included:

- **Track 1:** Sustainable Infrastructure Materials. This track included sessions on cementitious materials and composites, and their sustainability, environmental degradation of infrastructure materials, asphaltic materials, and multi-scale characterization and simulations;
- **Track 2:** Materials for Energy Extraction, Conversion, and Storage. This track included sessions on lightweight and high performance materials, energy storage materials, ferrocaloric and ferroelectric materials, nanomaterials for energy conversion, photovoltaics, and shape memory alloys; and
- **Track 3:** Computational Materials Design. This track included sessions on alloy and microstructure design, ab-initio materials modeling, computational approaches towards mechanical damage and environmental degradation, and modeling materials across the scales.

The congress consisted of all-conference sessions and parallel sessions that integrated 3 keynote and 14 invited presentations from international experts, 93 contributed presentations, and 62 poster presentations. From the poster session, outstanding posters were selected for awards, which were presented to the authors at the congress banquet.

The 56 papers presented in these proceedings are divided into five sections: (1) Sustainable Infrastructure Materials; (2) Computational Materials Design; (3) Materials for Energy Conversion and Storage; (4) Lightweight and High Performance Materials; and (5) Materials for Energy Extraction and Storage: Shape Memory Alloys. These manuscripts represent a cross section of the

presentations and discussions from this congress. It is our hope that the MEMA 2015 congress and these proceedings will provide new knowledge base for enhancing design, sustainability, and functionality of materials that are of interest for the Middle East and Mediterranean region; broaden the collaboration between the region scientists, industry, and the rest of the world; and ultimately help industry design and produce new materials more efficiently and effectively.

The organizers would like to thank all individuals and organizations that supported this congress. Special thanks are given to the Gold Sponsors of the congress: Qatar Petrochemical Company (QAPCO), and Qatar Foundation.

EDITORS/ORGANIZERS



Ibrahim Karaman

Ibrahim Karaman received his Ph.D. from University of Illinois at Urbana-Champaign in 2000. He joined the faculty of the Department of Mechanical Engineering at Texas A&M University in 2000. He was promoted to the rank of Professor in 2011. He has served as the Chair of the Interdisciplinary Graduate Program in Materials Science and Engineering (MSEN) from 2010 to 2013. The MSEN program became a new department in 2013. Dr. Karaman currently serves as the head of the department. His main research interests are processing-microstructure-mechanical/functional property relationships in metallic materials including (1) ultrafine and nanocrystalline materials, and (2) conventional, high temperature, and magnetic shape memory alloys; micro-mechanical constitutive modeling of crystal plasticity; and twinning and martensitic phase transformation. Dr. Karaman has received several national and international awards including the NSF CAREER Award, ONR Young Investigator Award, The Robert Lansing Hardy Award from The Minerals, Metals & Materials Society (TMS), an Honorable Mention for the Early Career Faculty Fellow Award from TMS, and Gary Anderson Early Achievement Award from ASME and AIAA. He is an author or co-author of more than 190 refereed journal articles.



Raymundo Arróyave

Raymundo Arróyave obtained his B.S. degrees in Mechanical and Electrical Engineering from the Instituto Tecnológico y de Estudios Superiores de Monterrey (México) in 1996. He got his M.S. in Materials Science and Engineering in 2000 and his Ph.D. in Materials Science in 2004 from MIT. After a postdoc at Penn State, he joined the Department of Mechanical Engineering at Texas A&M University in 2006. Since August 2012, he has been a faculty member of the newly created Department of Materials Science and Engineering at Texas A&M University. Dr. Arróyave's area of expertise is in the field of computational materials science, with emphasis in computational thermodynamics and kinetics of materials. He and his group use different techniques across multiple scales to predict and understand the behavior of inorganic materials (metallic alloys and ceramics). The techniques range from *ab initio* methods, classical molecular dynamics, computational thermodynamics, as well as phase-field simulations. Over the past seven years, Dr. Arróyave and his group have been using these techniques to investigate a wide range of materials, such as high-temperature shape memory alloys, ferromagnetic shape memory alloys, hydrogen storage materials, materials for electric

interconnects in microelectronic packaging, novel steel alloys, as well as nuclear fuels for next-generation nuclear power plants. More recently, Dr. Arróyave has been collaborating with colleagues in the fields of microstructural design and design theory to develop inverse methods for the discovery and design of multi-component, multi-phase structural materials. Dr. Arróyave has been co-author of more than 70 publications in peer-reviewed journals, 15 conference proceedings, as well as close to 100 conference papers and 37 invited talks in the United States and abroad. In 2014 he was the recipient of the TMS-EMPMD Distinguished Service Award. Earlier in 2012 he was awarded the TEES Select Young Faculty Fellow Award by the College of Engineering at Texas A&M University. He also received Honorable Mention as an Early Career Faculty Fellow of TMS. In 2010 he was awarded the CAREER Award from NSF. Earlier (2006), he was awarded the Young Leader Professional Development Award from TMS. He has served as the Chair of the TMS Alloy Phases Committee, in which he is currently a member. He is currently the Vice-Chair of the ASM Alloy Phase Diagram Committee and is an active member in the ICME, Physics and Chemistry of Materials as well as other technical and non-technical committees at TMS. He has also chaired and co-chaired more than ten symposia at TMS and MS&T.



Eyad Masad

Eyad Masad is a professor in the Mechanical Engineering Program at Texas A&M at Qatar and the Zachry Department of Civil Engineering at Texas A&M. Dr. Masad's research focuses on microstructure characterization and constitutive modeling of materials, transport in porous media, granular mechanics, and image analysis techniques. He has active research groups and programs in the United States and in the State of Qatar. He has published more than 350 technical papers and reports. Dr. Masad is a fellow of the American Society of Civil Engineers (ASCE). He is the recipient of the Eisenhower Graduate Research Fellowship (1997) and the Eisenhower Faculty Fellowship in Transportation Engineering (1998) from the Federal Highway Administration. He received several university awards including the Zachry Award for Excellence in Teaching (2004), the ConocoPhillips Faculty Fellow Award for outstanding performance (2005), the Texas Transportation Institute/Trinity New Researcher Award (2006), the Halliburton Professorship Award for Scholarly Excellence in Engineering (2009), and the Dean's Meritorious Service Award (2010).

ACKNOWLEDGMENTS

The organizers/editors would like to acknowledge the contributions of a number of people without whom the MEMA 2015 Congress, and the proceedings, would not have been possible.

First, we would like to offer many thanks to the TMS staff who worked tirelessly in the organization of the congress and the editing of the proceedings. The local organizing committee and the staff of Texas A&M University Qatar put long hours and tremendous effort to arrange the logistics of the congress and for this we are also tremendously grateful.

Second, we want to thank the international advisory committee for their input in the planning of the congress, the promotion of the congress, and their participation in the congress. This international committee included: Thomas Zacharia, Committee Chair, Qatar Foundation, Qatar; Imad Al-Qadi, University of Illinois at Urbana-Champaign, USA; Yehia Bahei-El-Din, The British University in Egypt; Tahir Cagin, Texas A&M University, USA; M. Enokizono, Oita University, Japan; Zachary Grasley, Texas A&M University, USA; Tayssir Hamieh, Lebanese University, Lebanon; Peter Hewlett, British Board of Agreement and University of Dundee, UK; Nick Kanellopoulos, National Center for Scientific Research “Demokritos”, Greece; Marwan Khraisheh, Qatar Energy and Environment Research Institute, Qatar Foundation, Qatar; Dallas Little, Texas A&M University, USA; A.G. Mamalis, PC-NAE, Greece; Tasneem Pervez, Sultan Qaboos University, Oman; Tom Scarpas, Delft University of Technology, The Netherlands; Hussein Zbib, Washington State University, USA.

We would also like to thank the keynote and invited speakers for graciously agreeing to present their work as well as the other presenters for the contributions, ensuring the success of the congress.

Finally, we would like to acknowledge the financial support of all our sponsors, especially the Gold Sponsors of the congress: Qatar Petrochemical Company (QAPCO) and Qatar Foundation, as well as the U.S. National Science Foundation, through the International Institute for Multifunctional Materials for Energy Conversion (IIMEC) at Texas A&M University, Grant No. DMR 08-44082.

MEMA ORGANIZERS

Ibrahim Karaman, Texas A&M University
Raymundo Arróyave, Texas A&M University
Eyad Masad, Texas A&M University at Qatar

ADDITIONAL ORGANIZERS

Raymundo Arróyave, Texas A&M University
Eyad Masad, Texas A&M University at Qatar
Zoubeida Ounaies, Pennsylvania State University
Dimitris Lagoudas, Texas A&M University
Mohammed Khaleel, Qatar Environment and Energy
Research Institute (QEERI), Qatar Foundation
Mariam Al-Maadeed, Qatar University
Pradeep Sharma, University of Houston

LOCAL ORGANIZATION COMMITTEE AND INDUSTRY LIAISONS

Eyad Masad, Texas A&M University at Qatar
Mariam Al-Maadeed, Qatar University
Bilal Mansoor, Texas A&M University at Qatar
Georges Ayoub, Texas A&M University at Qatar
Aboubakr M. Abdullah, Qatar University
Srinath Iyengar, Texas A&M University at Qatar
Said Mansour, Qatar Environment and Energy
Research Institute (QEERI), Qatar Foundation
Abdulaziz Al Mathami, Qatar Petroleum
Chris Devadas, Hydro Aluminum Technology Centre – Qatar
Mabrouk Ouederni, Qatar Petrochemical Company – QAPCO
Wakeel Ahmed Khalid Ahmed, Qatar Steel

INTERNATIONAL ADVISORY COMMITTEE

Thomas Zacharia, Qatar Foundation, Committee Chair
Yehia Bahei-El-Din, The British University in Egypt
Tahir Cagin, Texas A&M University
Hussein Zbib, Washington State University
Imad Al-Qadi, University of Illinois at Urbana-Champaign
Tom Scarpas, Delft University of Technology
Zachary Grasley, Virginia Tech University
Dallas Little, Texas A&M University
Nick Kanellopoulos, National Center for Scientific Research “Demokritos”

Marwan Khraishch, Qatar Environment and Energy
Research Institute (QEERI), Qatar Foundation
Peter Hewlett, British Board of Agreement and University of Dundee
Tayssir Hamieh, Lebanese University
A.G. Mamalis, PC-NAE
M. Enokizono, Oita University
Tasneem Pervez, Sultan Qaboos University



MEMMA

**Sustainable
Infrastructure
Materials**

CORROSION CHALLENGES FOR THE OIL AND GAS INDUSTRY IN THE STATE OF QATAR

Roy Johnsen

Norwegian University of Science and Technology (NTNU), Richard Birkelands vei 2b, N-7491 Trondheim, Norway

Keywords; Qatar, oil and gas, corrosion, hydrocarbon mixture, aquifer water

Abstract

In Qatar oil and gas has been produced from onshore fields in more than 70 years, while the first offshore field delivered its first crude oil in 1965. Due to the atmospheric conditions in Qatar with periodically high humidity, high chloride content, dust/sand combined with the temperature variations, external corrosion is a big treat to the installations and connecting infrastructure. Internal corrosion in tubing, piping and process systems is also a challenge due to high H₂S content in the hydrocarbon mixture and exposure to corrosive aquifer water. To avoid corrosion different type of mitigations like application of coating, chemical treatment and material selection are important elements. This presentation will review the experiences with corrosion challenges for oil & gas installations in Qatar including some examples of corrosion failures that have been seen.

Introduction

The first oil well in the State of Qatar was spudded in October 1938. This was an onshore well – named Dukhan 1 – that produced 5.000 barrels per day in January 1940. The first offshore concessions were granted in 1949. However, due to political reasons the first commercial offshore fields - Idd Al-Shargi and Maydan Mahzam fields - were discovered in 1960. In 1970 the large Bul Hanin field were discovered and came on stream in 1972. In these early years major international oil companies were responsible for the exploration activities in Qatar. However, early 1970-ties, the State of Qatar got its independence from UK and in 1974 they nationalized the oil sector and established Qatar Petroleum (QP). During the coming years Qatar took full control over all oil and gas activities onshore and offshore and the international oil companies were “sent back home” for a period.

In 1991 Qatar intensified their focus on oil and gas exploration and production. This resulted in a boost in oil & gas production from existing and new discovered offshore fields. To assist QP in more efficient exploration and production, international oil companies like ExxonMobil, Occidental, Total, Shell and Maersk Oil were invited to participate in the activities. All these international operating companies have been active during the last years bringing both capital, technology and technical skills to develop and improve the oil and gas exploration and development in the Qatar.

The North Field (together with South Pars on the Iranian continental shelf) - the world's largest single non-associated gas field - located in the Arabian Gulf is shared between Qatar and Iran. The field holds an estimated 1,800 trillion cubic feet (51 trillion m³) of in-situ natural gas and some 50 billion barrels (7.9 billion m³) of natural gas condensates. The field was discovered in 1971 but the first gas was produced in 1991. Still the North Field is the main field for producing natural gas in Qatar.

Due to the easy access to huge amount of natural gas in Qatar and the demand for utilizing this gas commercially, the development of downstream industry to utilize the gas reserves have been a prioritized activity by the Qatar authorities. Big onshore petrochemical plants have been developed in two main regions as can be seen in Table I:

Table I. Overview of main onshore process plants in Qatar.

<i>Messaid Industrial City (south of Doha)</i>	<i>Ras Laffan Industrial City (north of Doha)</i>
Qatar Fertilizer Co. Ltd (QAFCO)	Liquefied Natural Gas (LNG) – QatarGas and RasGas
Qatar Chemical Company Ltd (Q-Chem)	Gas to Liquid (LNG) – Oryx GTL and Pearl GTL
Qatar Vinyl Company Ltd (QVC)	Gas processing
Qatar Petroleum (gas treatment)	Laffan refinery
Qatar Petroleum (refinery)	Power company
Power company	
Qatar Steel (steel production)	
Qatalum (aluminium production)	

The daily production volumes in Qatar in 2012 were:

- Gas 150*10⁹ Sm³
- Oil 1.5*10⁶ barrels

Operation conditions in Qatar

Atmospheric conditions

The *environmental conditions* in Qatar are a strong driver for *atmospheric corrosion* on metallic materials and *degradation of coatings*. It occurs when the surface is wetted by moisture formed due to rain, fog or condensation. Atmospheric corrosion is a complex process involving large number of interacting and constantly varying factors such as e.g. weather conditions, air pollutants, actual metal and surface condition. Studies have demonstrated that most atmospheric corrosion phenomena are an electrochemical nature. These corrosion phenomena are influenced by several environmental factors like [1,2]:

- Atmospheric pollution
- Airborne salinity
- Sand/dust
- Temperature
- Time of Wetness

A classification of the corrosivity of an atmosphere is given in ISO 9223 [3]. In this standard the corrosivity is divided into six classes – Category C1; Very low corrosivity, CX: Extreme corrosivity.

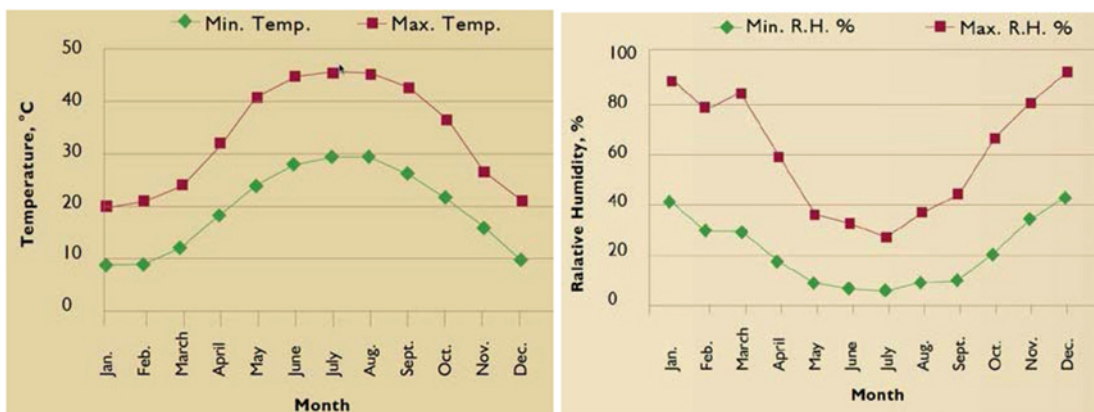


Figure 1 Average and maximum temperature and average and maximum relative humidity during the period 1997 to 2000 measured in Kuwait [2].

Hydrocarbon mixture

The composition of the hydrocarbon mixture varies between different fields and with type of field – oil reservoir or gas/condensate reservoir. One main challenge is the H₂S content of the reservoirs that can give partial pressure of H₂S in the range up to (and even above) 10 bar. This means that the reservoir fluid (hydrocarbon mixture) is characterized as sour according to ISO 15156 and materials have to be selected and qualified according to ISO 15156 – Part 2 and 3 [4]. Typical reservoir values are given in Table II.

Table II. Typical reservoir data for oil and gas/condensate wells in Qatar.

RESERVOIR	BHP [bar]	BHT [°C]	%CO ₂	%H ₂ S
Oil	250	100	5	2 - 8
Gas/condensate	360	100	2	1

Aquifer water

In Qatar natural aquifer reservoirs exists in the ground. These sources are used for pressure support to wells (Powered Water Injection – PWI). In addition many production wells go through the aquifer. Since these aquifers are used to dump produced water from oil & gas, they contain a significant amount of dissolved salts in addition to presence of H₂S, CO₂ and sulfate reducing bacteria (SRB). *Typical values are*; total dissolved solids up to 50.000 mg/l, chloride content up to 40.000 mg/l, pH ≈ 6.5, water temperature < 40°C, CO₂ < 80 mg/l, H₂S < 20 mg/l. They can also solved contain oxygen. Due to this composition the aquifer is often a corrosive fluid.

Main material challenges from earlier experiences

The biggest treat to the integrity of oil and gas facilities is corrosion and fatigue. This has been documented by different reports. Statoil presented one analysis based on all material related failure analysis done in-house during the period 1997 – 2010. Figure 2 Left shows a summery of the findings; 62% of all failures were caused by corrosion and fatigue with an equal potion of each failure mechanism. Qatar Petroleum (QP) did a similar evaluation of

reported material related failures during the period 2002 – 2006. The output from this evaluation – shown in Figure 2 Right – shows that for 29% of the failures corrosion was the root cause of failure.

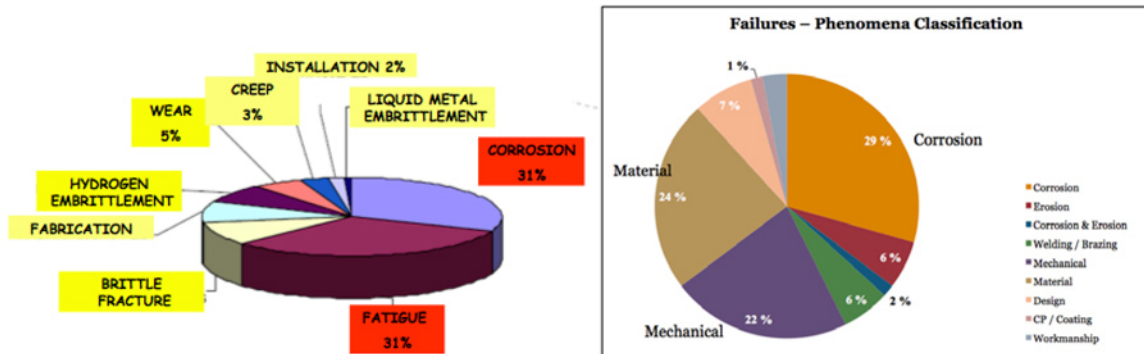


Figure 2. Results from evaluation of material related failures. Left: Statoil operated installation during the period 1997 – 2010. Right: QP operated installation during 2002 – 2006.

These analyses confirm the experiences from other oil & gas operators; Corrosion (and fatigue) is the biggest challenge for the integrity of oil and gas facilities. This is one main driver for ISO developing the standard “Petroleum, petrochemical and natural gas industries - Materials selection and corrosion control for oil and gas production systems” [5]. This document describes preferred materials for the different parts of the oil and gas production chain (not the downstream part, e.g. refinery) and is based on “best practice” from the major oil and gas operators in the world.

Corrosion challenges in Qatar

Corrosion under atmospheric conditions

Due to the special atmospheric conditions in Qatar external corrosion has been a major challenge for the operating companies – both onshore and offshore. For structural parts carbon steel is the main material choice. To prevent external corrosion carbon steel needs to be protected by a coating. The preferred solution is to apply an organic coating (often called a paint) to the structure to be protected. To secure a coating system with acceptable lifetime (min. 10 years maintenance interval), important factors are; selection of coating system, pre-preparation/cleaning before coating, application and curing. ISO 12944 “Paints and varnishes – Corrosion Protection of steel structures by protective paint systems” [6] is an important standard to follow to select the “best” coating system for a specific application.

However, due to the specific atmospheric conditions with periodically high temperature, high humidity, high chloride content, industrial pollution and periodically high content of sand/dust, degradation of a coating system followed by corrosion of the substrate material can be extremely high. Figure 3 shows two examples of damaged coating on carbon steel components. Heavy corrosion attacks can be seen on the carbon steel after the coating has lost its adhesion to the steel surface.

To repair damaged coating in the field and to achieve the same quality as for a component coated under controlled conditions in a factory is impossible. This means that as soon as a coating is damaged (or degraded) an intensive maintenance program needs to be put in place to avoid further corrosion degradation of the structure or component.



Figure 3. Damaged coating followed by corrosion of the carbon steel substrate material.

As mentioned earlier several elements are important to control to secure *an organic coating with acceptable lifetime*. Application of a metallic coating as an alternative to an organic coating (paint) has been more popular during the last years. To secure protection of the substrate material it is important to select a metallic coating that is less noble than the substrate material (normally carbon steel). Zinc and aluminium are two metals that are less noble than carbon steel. As long as a thin water film covers the surface, these alloys will act as a sacrificial anode and prevent corrosion of the carbon steel. Both Hot Dip Galvanizing (HDG), thermal sprayed zinc (TSZ) and thermal sprayed aluminium (TSA) can be used to apply the metallic coating.

Corrosion under insulation (CUI) is another major problem for all the industrial plants in Qatar. The challenge is that parts of the piping systems are externally heat insulated. It is very difficult to avoid water to penetrate the insulation and be entrapped in the insulation. Today it is normally required to paint a pipe/vessel beneath insulation. However, the paint will degrade followed by corrosion of the substrate material. Since inspection of the structure beneath the insulation is very difficult without removing the insulation, the result is often not-expected penetration of the pipe/vessel walls followed by serious leakage. Figure 4 shows an example of CUI on a carbon steel storage vessel. Original wall thickness was 16 mm, while the left picture shows that more than 50% of the wall thickness was corroded away when the inspection was executed.

One way to reduce the risk of initiation of corrosion under insulation is to apply thermal sprayed aluminium (TSA) instead of using organic coating (paint) on the substrate material. This has been a preferred solution for refineries for several years [7-10] and according to Houben [7] TSA coating with 250 μm thickness can be used in a wide temperature range -

40°C to 540°C and reach a design life of min. 30 years without maintenance. ExxonMobil has used this solution on the NGL plant in Ras Laffan with very good results.



Figure 4. Corrosion under insulation in a storage vessel made from carbon steel.

Even if carbon steel is the most used material, stainless steels are also used for special components/equipment mainly due to their improved corrosion resistance. Stainless steels are normally protected from corrosion by an oxide layer. However, under the atmospheric conditions that exist in Qatar – combination of high chloride content, presence of pollution (e.g. SO_4 , H_2S) and high temperature – the oxide layer can be degraded. The result is then excessive localized corrosion on stainless steel. *Chloride Stress Corrosion Cracking (CSCC)* is the most severe type of corrosion on stainless steel, but pitting and crevice corrosion can also result in leakages and loss of technical integrity. CSCC to occur requires i) a susceptible material, ii) local stresses in the material, iii) pitting/crevice corrosion. Several failures due to CSCC have been reported in Qatar [11, 12]. Most of the failures are related to the use of lower alloyed stainless steels like AISI 304 (UNS S30400) and AISI 316 (UNS S31600). Bolts, screws, pipes and vessels are typical components/equipment that have suffered from CSCC. The “easiest” way to prevent CSCC to occur is to select an alloy that is resistant against CSCC under the actual conditions. Alternative stainless steel alloys are; 904L, 22% Cr duplex stainless steel, 25% Cr super duplex stainless steel, 6Mo austenitic stainless steel, Alloy 625. *However, be aware that all these alloys have limitations regarding temperature and chloride content.* One important lessons learned: Do not use AISI 304 or AISI 316 in components that are exposed under atmospheric conditions and have local stresses (residual stress from welding, due to temperature, load)!

Corrosion in hydrocarbon environment

A hydrocarbon mixture containing CO_2 and H_2S is *not corrosive* as long as *water is not present*. However, the hydrocarbon mixture always contains water when it is retrieved from the reservoir – either formation water or condensed water. This means that the hydrocarbon mixture is corrosive. The corrosivity depends on parameters like pCO_2 , pH_2S , acid species,

pH, bicarbonate, temperature, water content, chloride content, flow conditions. Two degradation mechanisms are most important; i) Corrosion, ii) Hydrogen embrittlement [5]. Compared to other regions – e.g. the North Sea, Gulf of Mexico, Brazil – the content of H₂S in the hydrocarbon mixture is very high (see Table 1). Despite this high H₂S content, *carbon steel* is used for most of the tubing, production piping and pipelines without suffering corrosion. The main reason for this is the build up of a dense protective iron sulfide (FeS) scale on the surface. As long as this FeS scale is intact uniform and pitting corrosion will be reduced to an acceptable value (but, not completely prevented) [13]. However, if the FeS scale locally is damaged/removed, high corrosion rates can occur in these areas with bare steel due to a galvanic effect between FeS scale (cathode) and the bare steel (anode). To reduce the corrosion susceptibility mitigation through the use of corrosion inhibitor is also used for some wells.

Corrosion in production wells has shown to be a challenge. This is due to the fact that steel (API Spec. 5CT grade L80) is used as tubing material corrosion is a potential problem due to the composition of the hydrocarbon mixture. As long as a protective FeS scale is present on the tubing surface, corrosion will be kept at an acceptable value. Experiences have shown that the stability of a FeS scale in a tubing varies along the tubing. *This is due to the fact that both the composition of the hydrocarbon mixture changes along the tubing and not at least the flow conditions.* Another important element is the lack of reliable inspection and corrosion monitoring methods for tubing's. Existing multi-finger caliper tools can give direct quantitative measurements of the inner tubing walls. The caliper readings can be translated into wall thickness readings and assumptions around external conditions of the tubing. However, these assumptions often entail a high degree of uncertainty. A mechanical caliper tool can also damage a FeS scale on the tubing surface and increase the corrosion rate in these areas. Magnetic flux leakage tools can also be used to measure thickness loss as well as localized corrosion on the inner and outer tubing surface.

Several operators have experienced serious local corrosion attacks on tubing – in worst cases penetrating the tubing wall and force sour fluids into the annulus between the tubing and the casing¹³. This can give increased corrosion on the on the external of the tubing surface and on the casing. Figure 5 shows external corrosion on a tubing with the worst corrosion attack penetrating the tubing. The Right picture indicates that the penetration started from the outside. The *root cause* here was local corrosion from the tubing inside forcing hydrocarbon mixture into the annulus.



Figure 5. Tubing corrosion – Left: External corrosion including a penetration (hole). Right: The hole seen from the inside of the tubing.

Corrosion in aquifer water

External casing corrosion has been the main threat with the aquifer water¹⁴. For some wells the casing goes through an aquifer before the well again enters the solid ground down to hit the reservoir. To avoid external corrosion on the casing, special mitigation actions have to be taken. The most frequently used method is to apply a dense concrete coating on the outside of the tubing. As long as this concrete coating prevent water to penetrate and to hit the casing surface, corrosion will be prevented. If not prevented, the casing can be penetrated by corrosion and aquifer water will come into the annulus causing corrosion problem for the casing/tubing.

Corrosion in the well and the surface equipment is another challenge with the aquifer water. Corrosion in the down hole tubing is one of the serious and costly problems encountered in the field. Alzahrani et.a. [14] has presented a figure showing casing/tubing leak history in one of their field due to exposure to aquifer water. *During the period 1998 – 2006, they report 18 leaking wells.*

Due to the high corrosivity of aquifer water a detailed Corrosion Management Program needs to be put in place. This program should at least include; i) Risk Assessment including Risk Based Inspection (RBI), ii) Corrosion Mitigation Plan, iii) Corrosion Monitoring Plan, iv) Process Monitoring Plan, v) Inspection Plan, vi) Key Performance Indicators (KPI), vii) Plan for System Management.

Corrosion in seawater

Seawater is a very corrosive fluid due to the combination of high chloride content and oxygen. Seawater is used for several services – e.g. cooling water, fire water, fresh water generation – in a process plant. To avoid serious corrosion problems when exposed to seawater, ISO 21457 [5] lists the following alternative materials for use in chlorinated seawater; 25% Cr super duplex stainless steel/6Mo-austenitic stainless steel (max. 20⁰C), Inconel 625 (max. 30⁰C), titanium, Glass Fiber Reinforced Plastic (GRE).

In Qatar the seawater will have temperature above 20⁰C most of the year. Selection of a material with documented properties under these conditions is very important to avoid unwanted corrosion problems. Experiences when using AISI 316 or 22% Cr duplex stainless steel for seawater applications have shown that serious pitting and/or crevice corrosion have occurred and damaged the integrity of a system.

Carbon steel exposed to seawater will also suffer from corrosion. But contrary to stainless steel that suffers from pitting and/or crevice corrosion in seawater, the attack on carbon steel will be more uniform with insulated pits. If accounting for this during the design stage by adding a Corrosion Allowance (CA) and/or apply cathodic protection (normally combined with paint), carbon steel in contact with seawater can be an economical solution. This is the case for offshore structures.

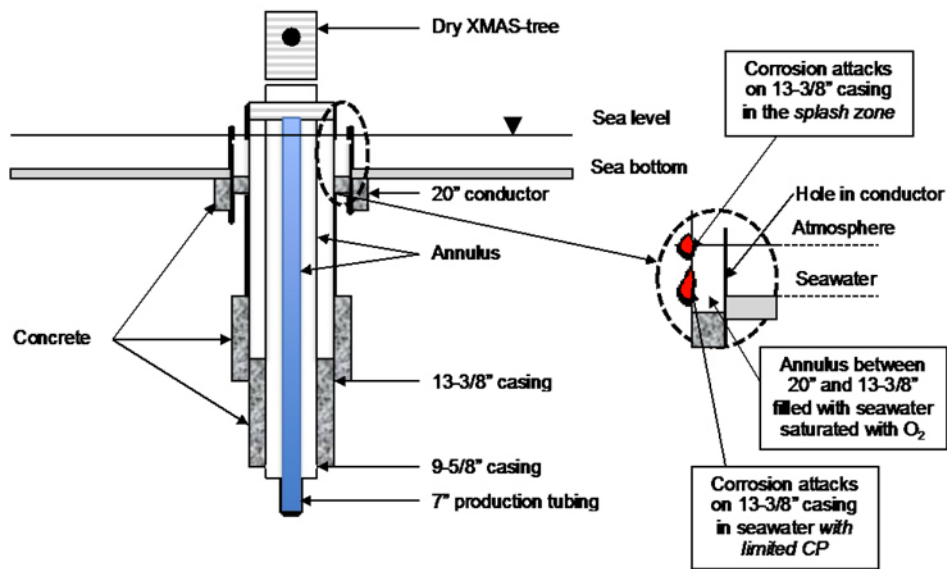


Figure 6. Schematic drawing of dry wellhead offshore Qatar. Serious corrosion on 13-3/8 casing due to limited effect of the CP system.

Offshore Qatar the water is shallow – max. water depth 50 m. This means that wells are completed with dry XMAS trees at surface on wellhead jackets. Offshore wells are constructed with 20” conductor casing, while the wellhead itself is installed on 13-3/8” outer casing. A window is cut in the 20” casing to monitor cement return for 13-3/8” outer casing protection. Due to this that seawater will fill annulus between the 13-3/8” casing and 20” conductor. The level of seawater stays inside the 20” conductor at splash zone level through the communication with cut window at sea bed, see Figure 6. A cathodic protection (CP) system is installed to protect the wellhead jacket structure and the 13-3/8” conductor (outside) and 20” conductor (inside and outside) from corrosion.

Qatar Petroleum has reported one failure due to corroded casing in seawater [15]. Figure 6 includes a schematic presentation of the corroded area on the 13-3/8” casing. As can be seen from the figure the outer of the 13-3/8” casing suffered from serious corrosion attacks in two regions; i) in the splash zone and ii) a region below the seawater level. The most serious corrosion attacks occurred in the splash zone. The corrosion resulted in wall thinning finally ending in fracture due to high stress in the remaining conductor wall. The main reason for the corrosion attack in the splash zone was lack of coating and limited effect of the CP system. Another contributing factor was the temperature of the casing that could reach 60°C due to the production fluid inside the tubing/casing. The pattern of the corrosion attack - highest corrosion rate in the splash zone, less corrosion just below the water level, increased corrosion rate further down and finally reduced corrosion in the bottom - can easily be explained with a combination of the effect of the CP system inside an annulus and reduction of oxygen deeper into the annulus due to oxygen consumption as part of the corrosion reaction. To avoid future similar problem with the actual well Qatar Petroleum decided to fill the actual annulus with concrete to remove the seawater from the casing surface.

References

1. Christopher Leygraf, Thomas Graedel; Atmospheric corrosion ISBN: 978-0-471-37219-6.
2. Atlas of Atmospheric corrosion of metals in Kuwait, Kuwait Institute for Scientific Research, 2009
3. ISO 9223:2012 Corrosion of metals and alloys -- Corrosivity of atmospheres -- Classification, determination and estimation
4. ISO 15156:2009 Petroleum and natural gas industries -- Materials for use in H₂S-containing environments in oil and gas production -- Part 1: General principles for selection of cracking-resistant materials, Part 2: Cracking-resistant carbon and low-alloy steels, and the use of cast irons, Part 3: Cracking-resistant CRAs (corrosion-resistant alloys) and other alloys
5. ISO 21457:2010 Petroleum, petrochemical and natural gas industries -- Materials selection and corrosion control for oil and gas production systems
6. ISO 12944:1998 Paints and varnishes -- Corrosion protection of steel structures by protective paint systems -- Part 1 to Part 8.
7. John Houben, ExxonMobil; "TSA Implementation – Learnings from project deployment". Presented at Eurocorr 2011 during WP 15 Corrosion in the Refinery Industry meeting. Stockholm, Sweden.
8. NORSOK M-501 Surface preparation and protective coating, ed. 6, 2012
9. NACE RP0198-98 (2004) The Control of Corrosion Under Thermal Insulation and Fireproofing Materials - A Systems Approach.
10. Corrosion under insulation (CUI) guidelines - EFC publication #55, ISBN 978 1 84569 423 4
11. G. Bharathan, S. Al Latifi; Case study of Chloride Stress Corrosion Cracking at Gas Recycling Plant, Dukhan – Theories and Practicality's. SPE paper 15611 presented in Doha Qatar 14-16 May 2012.
12. J.V.D. Murty, I. A. Muzghi; Materials and Corrosion in LNG Industry – Our Experiences. IPTC 17222 presented at the IPT Conference in Doha Qatar 20-22 January 2014
13. L.B. Morshidi, M.Z. Farooqui, M.A. Bugti, A. Kumar, S.K. Desai, J.L. Pacheco; An evaluation of production casing corrosion due to ingress of sour gas in the tubing-casing annulus. IPTC 17423 presented at the IPT Conference in Doha, Qatar 20-22 January 2014.
14. M. Alzahrani, K. Senusi, D. Lewis, A. Aty, F. Shinaiber; Effective wells Corrosion Mitigation in two Major Midle East Fields: A Case Study. IPTC 17399 presented at the IPT Conference in Doha, Qatar 20-22 January 2014.
15. S.K. Pandey, S. Rana, A. Fakhroo; Well Structure Integrity Threat Due to near Surface Corrosion of Outer Casing at Offshore Wells. IPTC 17557 presented at the IPT Conference in Doha, Qatar 20-22 January 2014.

UTILISING FINE AND COARSE RECYCLED AGGREGATES FROM THE GULF REGION IN CONCRETE

M Rod Jones, Judith E Halliday, Laszlo Csetenyi, Li Zheng and N Strompinis

University of Dundee, Concrete Technology Unit,
School of Engineering, Physics and Mathematics, Dundee UK

Keywords: Synthetic Sand, Recycled Coarse Aggregates, Concrete

Abstract

This paper explores the feasibility in utilising materials generated from C&DW to produce a 'green' concrete. The two materials that are considered here are, (i) up-sizing silt-size material generated from recycled aggregates to produce a synthetic silt-sand and (ii) processed recycled coarse aggregates (RA) sourced from a Gulf Region landfill site. The work has demonstrated that there is potential for utilising silt wastes into foamed concrete, which can then be crushed to a sand-sized material suitable for use in concrete, however the porous nature of the material has highlighted that the water demand of this RA is high. RAs were characterised to BS EN 12620 and found suitable for use in concrete. The effect of RA on concrete properties is minimal when used up to 35% replacement levels, provided that they are pre-soaked.

Introduction

There is an increasing global demand for using alternative "green" construction materials, with the pressure be even greater for countries under rapid infrastructure development. Moreover, the Middle East region has recently concentrated in major construction projects over the last 10 years. However, the problems of such projects carried out today are two-fold, namely; (i) with current reserves of quality sand and aggregates, for use in concrete construction, diminishing and the majority of local quality natural aggregate being limited and therefore, aggregates are imported from neighbouring countries and (ii) large quantities of construction and demolition wastes (C&DW) are being generated and with only 50% of this may be recycled into aggregates suitable for construction [1].

Although over the past decade there have been major strides in minimising, reusing and recycling of wastes, large quantities of materials still have to be landfilled. Of these, silt-sized materials (i.e. <1mm) are a particular problem. Conservatively, silt-sized waste arising generate 20% of the total crushed rock production (MPA Sustainability Development Report, 2013 [2]). Small amounts of these silts are recycled as a filler in bituminous mixes but the majority are too difficult to reuse, as they are generally volume unstable in fills and BS EN 12620 (2013) restricts this content to <3%, if deemed 'harmful' (i.e. containing clay minerals). If used in concrete they generally increase water demand, and require additional chemical admixtures to maintain workability and adversely affect volume stability [3-6].

This paper explores the feasibility in utilizing materials generated from C&DW to produce 'greener' concrete mixes and products. The two materials that we focused on were, (i) up-sizing silt-size material generated from recycled aggregates to produce a synthetic silt-sand and (ii) processed recycled coarse aggregates (RA). The main aim of the whole project is to incorporate

CSA cement with recycled materials to produce a 100% 'green' concrete (although outside the remit of this paper).

Experimental Programme

Synthetic Sand Production: Silt from processed RAs from a landfill site in the Gulf Region were used. A stockpiled fly ash, obtained from a UK power station, was used as a reference material. The silts were characterised with respect to their physical properties (maximum particle size, particle density, moisture content and specific surface area) and chemical and compositional properties (sulfate and chloride contents, loss-on-ignition and SEM images). The basis of the process was to incorporate the silt initially into a foamed concrete mix at a Portland cement/Silt ratio of 1:3, with enough water added to ensure workability of the base mix. The foamed concrete was crushed to sand size using a standard laboratory jaw-crusher and the resulting material was placed in a CO₂ chamber for 10 days to carbonate to improve mechanical properties.

Recycled Aggregate (RA) characterisation: The physical (composition, grading, density, water absorption), chemical (SO₃ and Cl contents) and mechanical (Los Angeles value, Flakiness Index and drying shrinkage) properties of RAs were carried out on two size fractions (10mm and 20mm) in order to classify the RAs and determine their suitability for concrete. The processed RA was collected from the same landfill site as the silt material.

Effect of RA on Concrete Properties: The effect of replacing 20 and 35% of coarse natural aggregates with RA was determined by testing the fresh properties (slump and plastic density), engineering properties (compressive, flexural and tensile strength) and permeability properties (ISAT-10 and sorptivity). Limestone and gabbro aggregates used extensively throughout the Middle East were used as a reference.

Test Methods and Process Methodologies

Up-sizing via Incorporation in Foamed Concrete

This was carried out by incorporating the silts into the foamed concrete base mix using a slow speed rotary drum mixer using a pre-formed protein-based foam to achieve a target plastic density. The workability of foamed concrete was assessed in terms of slump flow spread [7] and plastic density using BS EN 12350-6 [8]. The foamed concrete was then cast into standard cube moulds, covered for 24hrs, then demoulded and sealed cured for 14 days. Compressive cube strengths and hardened density of foamed concrete were measured in accordance with BS EN 12390-3 [9] and BS EN 12390-7 [10] respectively.

Material Characterisation

Silt: Particle density of silt was measured using the BS EN 12620 [11] method for fine aggregates and moisture content in accordance with the procedure described in BS EN1097-5 [12]. A Malvern 2000 particle size analyser was used to determine the particle size distribution of the ashes. Specific surface area of silts were carried out using BET nitrogen adsorption and their typical microstructural appearance determined by SEM. The loss-on-ignition (LOI) was determined by igniting approximately 1.0g of material in a furnace at 975°C for 1 hour [13].

Recycled Aggregates: The composition and fines content were calculated in accordance with BS EN 933-1 [14] whilst the water absorption and particle density followed BS EN 1097-6 [15].

Mechanical properties were determined in accordance with BS EN 1097-2 [16] (Los Angeles) and BS EN 933-3 [17] (Flakiness Index) and total SO₃ was determined using a Panalytical MagiX fluorescence spectrometer with an RhK α source. Acid-soluble chloride was determined to BS EN 1744-5 [18]. Drying shrinkage tests were carried out using the BS EN 1367-4 [19] method.

Concrete Properties

Concrete mixes were designed generally following the BRE procedure [20]. Concrete was mixed following procedures in BS 1881-125 [21] and consistency and plastic density was determined to BS EN 12350-2 [22] and BS EN 12350-6 [8] methods respectively. Compressive strength was tested at 3, 7 and 28 days in accordance with BS EN 12390-3 [10] and flexural and tensile strength following BS EN 12390-5 [23] and BS EN 12390-6 [24]. ISAT and water absorption tests were carried out in accordance with BS 1881-208 [25] and BS 1881-122 [26] respectively to determine permeation properties.

Experimental results

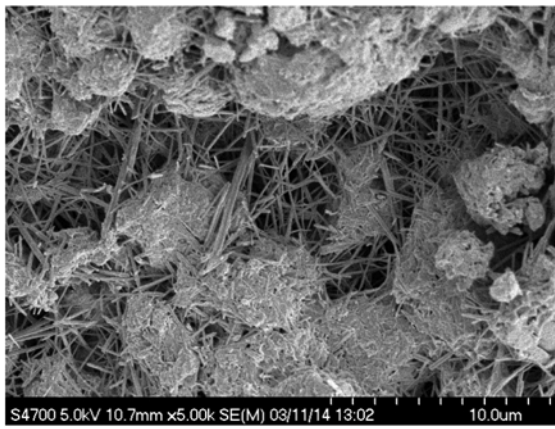
Foamed-sand production

The silt characteristics are given in Table I and SEM images are shown in Figure 1. The RA silt had a maximum particle size of 125 μ m and a particle density of 2560kg/m³. The stockpiled FA was much coarser, with maximum particle size being 340 μ m. The material was sprayed with water to reduce dust during transportation and the moisture content was found to be 19.0% for RA and 10% for stockpiled FA. The specific surface area was relatively high compared to that of stockpiled FA. The RA silt had a sulfate content of 2.5%, suggesting that there was Portland cement paste present, which is supported by ettringite, observed using SEM in Figure 1 (shown as fine ‘needle’ like crystals).

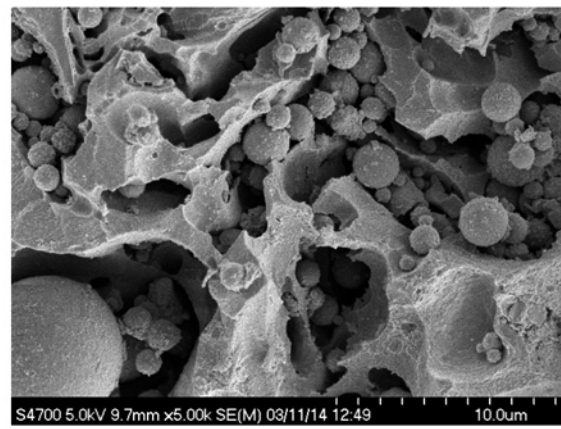
Table I. Raw Silt Characteristics

Property	Maximum particle size, μ m	Particle density, kg/m ³	Moisture content, % by mass	Specific surface area, m ² /g	Loss-on-ignition, % by mass	Total chemical content, % by mass [§]	
						SO ₃	Cl
RA Silt	125	2560	19.0	19.6	23.0	2.5	0.6
Stockpiled FA	340	2060	10.0	8.0	15.3	2.0	nd*

*not detected, [§]determined by XRFs



A) RA



B) Stockpiled FA

Figure 1. General Micro-Structure of Raw Silts

The test materials were added to the foamed concrete base mix and foam was added to give a target plastic density of 1300 kg/m³ (Table II). The properties of the resulting foam concrete are given in Table III. The water required to achieve a flow of 240mm for RA silt was considerably more than that of stockpiled FA, suggesting that particle shape and size alone is not enough to characterise this material in terms of flow properties. This issue was reflected in the total surface area for RA silt shown in Table I and the mineralogical composition shown in Figure 1.

Table II. Foam Concrete Constituent Mix Proportions

Silt Type 1:3 PC/Silt ratio	Mix Proportions, kg/m ³				Total w/c ratio*	Total w/f ratio ^s
	Cement	Silt	Total water	Foam		
RA	195	585	560	26	2.87	0.72
Stockpiled FA	225	675	405	27	1.80	0.45

*w/c: water/cement, ^sw/f: water/fines (cement+silt)

The compressive strength of foamed concrete has a general relationship with the cement/silt ratio and the total water/cement ratio. Results show that in this instant the RA required too much water and as a result did not achieve a sufficient strength at 14 days for crushing. Further work on pre-treatment methods with (or without) chemical admixtures is required to ensure that the water demand is kept to a minimum. Figure 2 shows a typical ‘crushed’ foamed concrete containing stockpiled FA.

Table III. Fresh and Hardened Properties of Silt Foamed Concrete

Silt Type 1:3 PC/Silt ratio	Slump flow, mm	Density, kg/m ³		Compressive cube strength, N/mm ² *		
		Plastic	Hardened* (28 days)	7 days	14 days	28 days
RA	235	1290	1255	0.4	0.4	0.4
Stockpiled FA	245	1300	1200	1.0	1.4	2.0

*sealed cured



Figure 2. Typical Ungraded Silt Sand (Stockpiled FA 1:3 cement/silt ratio)

Recycled Aggregate

Physical Properties

Table IV gives the BS EN 12620 (2013) [11] limits for coarse RA properties and the results of the tests on recovered RAs.

BS EN 12620 states that fines content is declared, as an excess of fines can lead to consistency and shrinkage problems when used in concrete. The fines contents of these aggregates are less than 1.5%.

BS EN 12620 classifies two types of recycled aggregate depending on their composition. Type A has a 95% R_{cu} ($R_c + R_u$) [R_c = concrete + R_u = unbound aggregate] content, as these are deemed to be the materials with the best mechanical properties, and Type B with 70% R_{cu} ($R_c + R_u$) content. Table IV gives the content of R_{cu} ($R_c + R_u$) content at above 95%, therefore both size fractions are classified as Type A. The RAs used in this paper did not contain any such material (as shown in Figure 3).

In accordance with BS EN 12620, RAs can be classified as Type A, as their oven-dried densities are $>2100 \text{ kg/m}^3$. The water absorption values for 10mm and 20mm size fraction were relatively high at 4.9% and 5.9% respectively. BS EN Standards do not limit the absorption values (although values must be declared).

Table IV. Physical-chemical Characteristics of Coarse RAs

Property	RA		Limits/ Recommendations
	20 mm	10 mm	BS EN 12620 [11]
Composition (R_{cu}), %	99.0	99.0	Type A: R_{c90} , R_{cu95} , R_{b10-} , FL_{2-} , XR_{g1-} Type B: R_{c50} , R_{cu70} , R_{b30-} , FL_{2-} , XR_{g2-}
Shell Content	None	None	3% max
Fines content, % by mass <63mm	$f_{1.5}$	$f_{1.5}$	Declare
Apparent particle density, kg/m^3	2785	2720	>2100(A) ¹⁾ >1700(B)
Particle density, kg/m^3 SSD	2580	2480	
Particle density, kg/m^3 oven-dried	2460	2350	
Water Absorption, %	4.9	5.9	Declare
Flakiness index	FI_{10}	FI_{10}	50
LA Value	LA_{25}		50
Drying shrinkage, %	0.069		0.075
Acid-soluble chlorides, %	0.0	0.0	0.01-1% ²⁾
Acid-soluble sulfates, % ³⁾	<0.48	<0.70	0.2, 0.8

1) Standard applied only in oven dried condition for Type A and B of RA

2) Provided the value is below 0.01%, the standard allows to use for in concrete

3) Total sulfates determined using XRFS

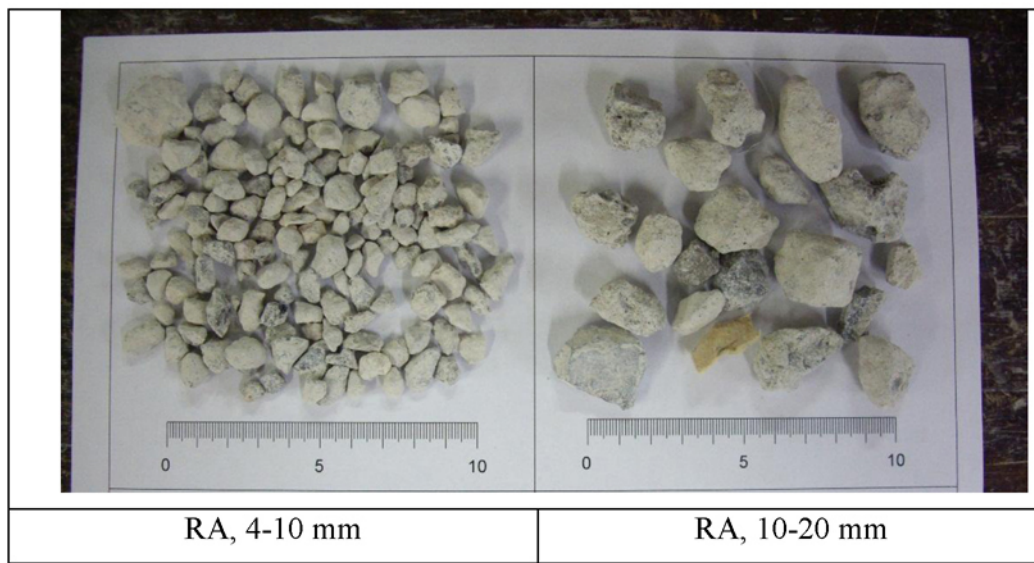


Figure 3. General Appearance of Processed RA

Flat shaped aggregates can cause problems with bleed water and air voids forming underneath particles and in both primary and recycled aggregates this is assessed by the Flakiness Index (FI). BS EN 12620 limits this to 50 for aggregates. The mechanical properties of aggregates influence suitability for different applications, e.g., pavement construction or concrete subjected to high wear. The Los Angeles (LA) test combines attrition and abrasion and the research has shown good correlation with the actual wear of aggregate when used in concrete and with compressive strength. BS EN 12620 gives a maximum LA value of 50 for recycled aggregates. The FI value of 10 and LA values of 25 and therefore, RAs conform to Standard (Table IV).

Aggregate characteristics, particularly shrinkage strain influence concrete durability and structural performance [27] and aggregates with high absorption values generally increase shrinkage. BS EN 12620 limits shrinkage to 0.075% and results given in Table IV show that the RA complies with this requirement.

Chemical Properties

The chloride content of concrete is normally limited to between 0.2-1.0% by mass of cement based on the sum of the contributions from all constituents. Although this is only pertaining to structural concrete. BS EN 12620 also includes categories for recycled aggregate based on acid-soluble sulfates, as these can lead to volume instability in hardened concrete, with two categories being SS0.2 and SS0.8 (% by mass). Table IV gives the acid-soluble Cl and SO₃ contents and both were found to be lower than limits set by BS EN Standards. It should be noted that the results given in Table IV are for total SO₃, as determined using XRFS, hence the acid-soluble concentrations would be lower and therefore may conform to the Standard limits. Figure 4 shows the XRD traces for RAs, and belite, portlandite, gypsum, ettringite, calcite, dolomite, quartz, albite and kaolinite were found to be the most prominent, which are typical of a recycled concrete aggregate. From the components observed, the sulfate containing phases are likely to be associated with gypsum and ettringite.

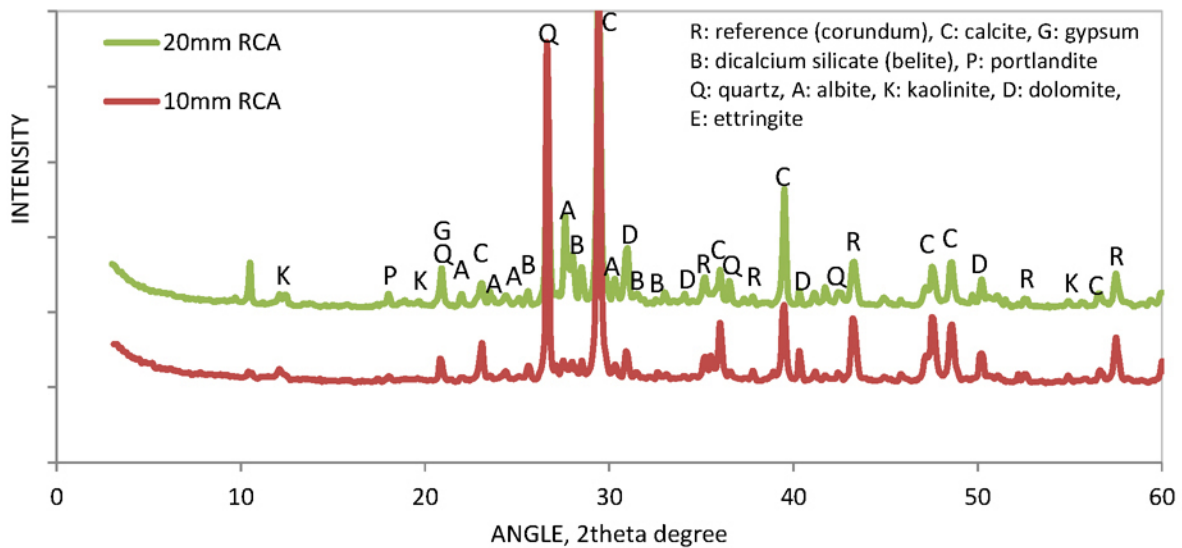


Figure 4. XRD Trace for RAs

Concrete Properties

The mix proportions are given in Table V and results are shown in Table VI.

Table V. Mix Constituent Proportions of Concrete Containing Coarse RA

Replacement level, % by mass	Constituent, kg/m ³							SP, %*
	PC	Water	Sand	Coarse aggregates				
				10mm		20mm		
				NA	RCA	NA	RCA	
0	300	180	865	350	-	705	-	0.3
20	300	180	865	280	70	565	140	0.3
35	300	180	865	230	120	460	245	0.3

*Glenium 51 (dosage: % by batch weight of cement)

Table VI. Properties of Concrete Containing Coarse RA

Properties	Limestone			Gabbro		
	RA content, % by mass					
	0	20	35	0	20	35
Slump, mm	95	80	55	110	75	65
Plastic density, kg/m ³	2390	2370	2370	2400	2370	2360
Compressive strength, N/mm ²						
3 days	29.5	32.0	30.5	30.0	28.0	26.5
7 days	36.0	40.0	35.0	39.0	37.0	36.0
28 days	43.0	44.0	42.0	45.0	43.0	41.0
Flexural strength, N/mm ²	5.8	6.1	5.4	6.2	5.5	5.2
Splitting tensile strength, N/mm ²	4.6	4.6	4.7	4.5	4.0	3.9
ISAT-10 minute, ml/m ² /s	5.8	5.8	5.9	5.8	5.8	5.9
Sorptivity coefficient	0.35	0.40	0.40	0.35	0.45	0.45

Fresh Properties

The consistence of concrete was found to decrease as the replacement level was increased, but this was probably due to an incorrect batching issue. It was noted that establishing the saturated

surface dry density of these recycled aggregates was difficult. Thus, the batched free water content of these mixes was not achieved.

This issue can be eliminated by treating RA like a lightweight aggregate, and pre-soak the material for 24 hours prior to mixing. Further work is being carried out in Dundee to address this need.

Engineering Properties

The compressive strength results are given in Table VI. The findings show that whilst there is a slight decrease in strength as replacement levels reach 35%, this is minimal, and within the range of variability. Similar results were noted for both flexural and splitting tensile strength tested at 28 days.

Permeation Properties

Permeability of concrete is usually a function of the strength –with higher strengths resulting in lower permeability. As noted above, there was little difference when RAs were introduced (see Table VI).

Conclusions and Further Work

The research summarized here shows that, otherwise impossible to utilize silt wastes, can be up-sized to a sand-sized material suitable for use in concrete. This lightweight sand also sequesters CO₂ and could be used in non-structural precast products such as blocks. Not only will this protect natural sand deposits in the Gulf Region (and reduce dependence on imported material), but will also enhance thermal and acoustic properties of blocks, which is advantageous for housing. Together with colleagues in Aberdeen University, these applications are now being investigated.

The processed coarse RA, obtained from a landfill site, was found to conform to BS EN 12620 (2013) and therefore suitable for use in concrete. However, SO₃ content could be an issue. In further work with Aberdeen University, this is being investigated, to assess whether this phase does contribute to any long-term volume instability. In addition, research is being undertaken to utilize a new type of cement that can react favourably with any soluble sulfate phases in recycled aggregate and will be reported at a later date.

Using RA as a replacement of natural aggregate in concrete, was found to decrease the workability, and whilst this could be due to aggregate surface roughness and shape, it is more probable that the amount of free water absorbed during mixing was much higher than initially determined by following water absorption tests. This in turn has resulted in lowering the water/cement ratio of concretes containing RA and therefore enhancing the engineering and permeation properties. Further work into pre-treatment of RA prior to mixing will be required.

Acknowledgements

The Authors would like to acknowledge the support given by colleagues at the Engineering and Chemistry Departments at Aberdeen University (UK).

References

1. Al-Ansary, M and Iyengar, S R, 2013, Physiochemical characterization of coarse aggregates in Qatar for construction industry, *International Journal of Sustainable Built Environment*, 2, 27-40.
2. Mineral Products Associations (MPA), Sustainability Development Report, UK, 2013.
3. Çelik, T. and Marar, K., 1996, Effects of crushed stone silt on some properties of concrete. *Cement and Concrete Research*, 26, pp 1121-1130.
4. Dumitru I, Zdrilic, T and Smorchevsky G, 1999, The use of manufactured quarry fines in concrete, *International Center for Aggregates Research (ICAR), 7th Annual Symposium*, Sydney, Australia.
5. Katz, A and Baum, H, 2006, Effect of high levels of fines content on concrete properties, *ACI Materials Journal*, 103-M53, pp 474-482
6. Cho S-W, 2013, Effect of silt fines on the durability properties of concrete, *Journal of Applied Science and Engineering*, Vol. 16, No 4, pp 425-430
7. BS EN 12350-8, 2009, Testing fresh concrete: Flow spread, BSI, London, UK.
8. BS EN 12350-6, 2009, Testing fresh concrete: Density, BSI, London, UK.
9. BS EN 12390-3, 2009, Testing hardened concrete: Compressive strength of test specimens, BSI, London, UK.
10. BS EN 12390-7, 2009, Hardened density of test specimens, BSI, London, UK.
11. BS EN 12620, 2013, Aggregates for concrete, BSI, London, UK.
12. BS EN 1097-5, 2008, Tests for mechanical and physical properties of aggregates. Determination of the water content by drying in a ventilated oven, BSI, London, UK
13. BS EN 196-2, 2005, Methods of testing cement: Chemical analysis of cement, BSI London, UK.
14. BS EN 933-1, 2012, Tests for geometrical properties of aggregates. Determination of particle size distribution. Sieving method, BSI, London, UK
15. BS EN 1097-6, 2008, Test for mechanical and physical properties of aggregates. Determination of particle density and water absorption, BSI, London, UK
16. BS EN 1097-2, 2008, Tests for mechanical and physical properties of aggregates. Determination of the Los Angeles Value, BSI, London, UK
17. BS EN 933-3, 2012, Tests for geometrical properties of aggregates. Determination of particle shape. Flakiness index, BSI, London, UK
18. BS EN 1744-5, 2006, Tests for chemical properties of aggregates. Determination of acid soluble chloride salts, BSI, London, UK.
19. BS EN 1367-4, 2008, Tests for thermal and weathering properties of aggregate. Determination of drying shrinkage, BSI, London, UK
20. Teychenné, D. C., Franklin, R. E. and Erntroy, H. C., 1997, Design of normal concrete mixes, 2nd Edition, Building Research Establishment, UK
21. BS 1881-125, 2013, Concrete Testing. Methods for mixing and sampling fresh concrete, BSI, London, UK
22. BS EN 12350-2, 2009, Testing fresh concrete: Slump test, BSI, London, UK.
23. BS EN 12390-5, 2009, Testing hardened concrete: Flexural strength of test specimens, BSI, London, UK.
24. BS EN 12390-6, 2009, Testing hardened concrete: Tensile splitting strength of test specimens, BSI, London, UK.
25. BS 1881: Part 208, 1996, Recommendations for the determination of the initial surface absorption of concrete, BSI, London, UK.

26. BS 1881-122, 2011, Testing of concrete. Determination of water absorption, BSI, London, UK
27. Neville, A M, 2012, Properties of Concrete, 5th Edition, Longman, UK

Finite Element Simulation of the Response of No-Tension Materials

Alieh Alipour¹, and Tom Scarpas²

^{1,2}Section of Pavement Engineering

Faculty of Civil Engineering & Geosciences

Delft University of Technology

Address: Stevinweg 1, 2628 CN, Delft, The Netherlands.

Tel: +31152784669, Email: ¹A.Alipour@tudelft.nl ²A.Scarpas@tudelft.nl

Keywords: Granular materials; No-tension model; CAPA3D; Finite elements

Abstract

Unbound granular materials that are used at base layer of flexible pavement cannot resist tensile forces. These materials are called no-tension materials. In this paper, a modified strain-energy function was used to describe the constitutive behavior of granular materials to simulate flexible pavement within the finite element framework CAPA3D. The constitutive model was defined such that the positive stresses in principal directions were zero. Comparisons between the no-tension materials and linear elastic materials for different boundary conditions and geometries were presented in this paper. The results of FE analysis show that effect of using no-tension model for base layer on pavement performance is significant. The deformation at top and horizontal strain at the bottom of asphalt concrete layer are higher when the no-tension model is used.

Introduction

Predicting accurate pavement performance is one of the most important tasks for the pavement engineering community [1]. The non-linear, stress dependent response of granular materials typically used in pavement construction, necessitates the utilization of appropriate constitutive models capable of simulating the fundamental response characteristics of this type of materials.

In the context of the Finite Element method (FE) several constitutive models have been proposed by various researchers for simulation of the response of unbound granular materials and their influence on the overall pavement performance. Since unbound granular layers exhibit completely different strength and stiffness characteristics when subjected to tension and compression, a variety of techniques have been proposed to address this issue.

Some studies consider unbound granular materials as an anisotropic material [2, 3, 4]. Typical elastic anisotropic constitutive models may be adequate in describing the differences in material stiffness in the horizontal and vertical directions within a pavement layer, nevertheless, they cannot address the dependence of stiffness on the nature of the prevailing stress i.e. tension vs. compression.

Utilization of models based on the theory of anisotropic plasticity can introduce state of stress dependent differences in the stiffness characteristics of the material, but requires information which is typically way beyond that which is available to pavement designers and, the use of complicated nonlinear finite element analysis techniques.

An alternative to the use of anisotropic plasticity and nonlinear analysis techniques is the simulation of the low tensile response characteristics of granular materials by means of what is known as no-tension models. These are anisotropic elasticity models in which the stiffness of the material in each of the three principal axes is determined on the basis of the prevailing state of strain. Nguyen et. al. [5] used a modified strain energy function to model the no-tension characteristics of granular-like materials on the basis of principal stretches. They used the model to simulate a quasi-static test on ballast materials. The results showed that the influence of the no-tension model in a granular structure can indeed be significant [5].

The objective of this study is the evaluation of the contribution on the overall pavement response, of the simulation of the unbound granular material layers by means of the Nguyen et. al. [5] no-tension model. In the first part of the paper, a brief description of the constitutive model is presented followed by a numerical evaluation and comparison of its response characteristics versus a standard elastic model. Next, the results of FE simulations are presented for a two layer flexible pavement. The results show that overall deformations in the asphalt concrete (AC) and the base layer are higher when the base is modeled by means of a no-tension constitutive model.

Concept of no tension model

The perfectly no-tension material model assumes an idealized continuum made up of granules incapable of sustaining any tensile stress between them. On the other hand, the material is perfectly capable of sustaining uniaxial compressive stresses, Figure 1, [6].

Assume a uniaxial compression-tension test in which Hooke's law describes the uniaxial stress-strain relationship. In order to simulate the no-tension response, the constitutive law was modified as it is expressed in Eq. (1)

$$\begin{cases} \sigma = K\varepsilon & \text{if } \varepsilon \leq 0, \\ \sigma = 0 & \text{otherwise,} \end{cases} \quad (1)$$

Where σ , ε , and K are stress, strain, and material constant respectively.

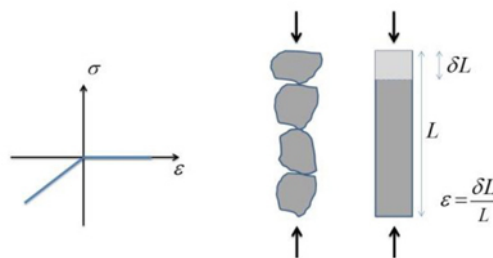


Figure 1. Concept of no-tension model for unbound granular materials

Similar to the 1D example, for a 3D case the constitutive law was adjusted such that in principal space the material does not resist against tension. Eq. (2) shows the normal stress acting on of any element with unit normal n_i , cannot be positive, and the 3x3 matrix σ_{ij} will be negative semi-definite [6].

$$\sigma_n = \sigma_{ij} n_i n_j \leq 0, \quad \forall n_i : n_i n_i = 1, \quad (i, j = X, Y, Z) \quad (2)$$

Hyperelastic model

In order to use a no-tension material in constitutive law which was used to describe the response of granular base, a hyperplastic material model was utilized and modified. This modification was such that in compression the material behaves like a normal hyperplastic, while in tension, it shows negligible strength.

In this study, the response of the standard elastic materials was simulated by means of a small strain hyperelastic model in which the strain energy function Ψ depended only on strains [7]

$$\Psi = \frac{1}{2}\lambda \left[\sum_{a=1}^3 \varepsilon_a \right]^2 + \sum_{a=1}^3 \mu [\varepsilon_a]^2 \quad (3)$$

where ε_a are the principal strains, and λ and μ are Lamé's constants.

No-tension model

To simulate the no-tension behavior of granular-like materials, the strain energy function that was introduced in previous section was modified [5] such that the tensile stresses in the material are always zero. The redefined strain energy function is

$$\Psi = \frac{1}{2}\lambda \left\{ \left[\sum_{a=1}^3 \varepsilon_a \right]^- \right\}^2 + \sum_{a=1}^3 \mu [\varepsilon_a^-]^2. \quad (4)$$

where the operation $(\phi)^-$ indicates the negative part of ϕ

$$\phi^- = \frac{1}{2}(\phi - |\phi|). \quad (5)$$

The net effect of the above choices is the removal of the stiffness and corresponding stress values along tensile principal strain material directions. Details of the model formulation and the evaluation of the tangent moduli can be found in [5] and [9].

Validation

The finite element system CAPA-3D [8] was utilized for evaluation of the fundamental model characteristics. The response of a cube was compared for a no-tension material and a hyperelastic material. As shown in Figure 2(a), a linearly increasing uniform pressure with a magnitude of 0.02 MPa in the Y direction and 0.04 MPa in the Z direction was applied on a cube whose faces in the X-Z, X-Y and Y-Z planes were restrained against motion in the Y, Z and X directions respectively. The values of λ and μ for this material were 1153.84 MPa and 769.23 MPa respectively.

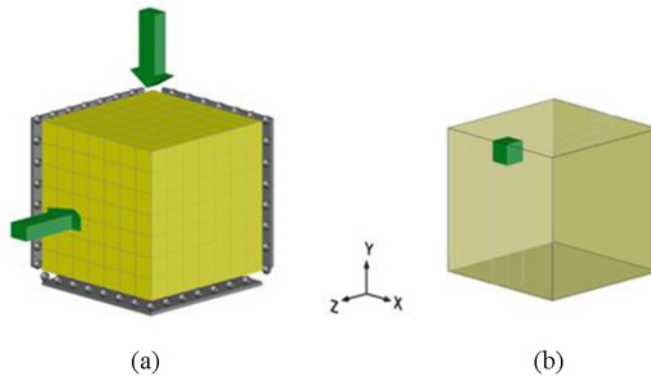


Figure 2. (a) The boundary condition and load direction for a cube, (b) position of the element

The results of strains for a point in the middle of an element near the top face of the cube, Figure 2(b), are shown in Figures 3 and 4. It can be seen that the no-tension material demonstrates a much more flexible response than a standard hyperelastic material.

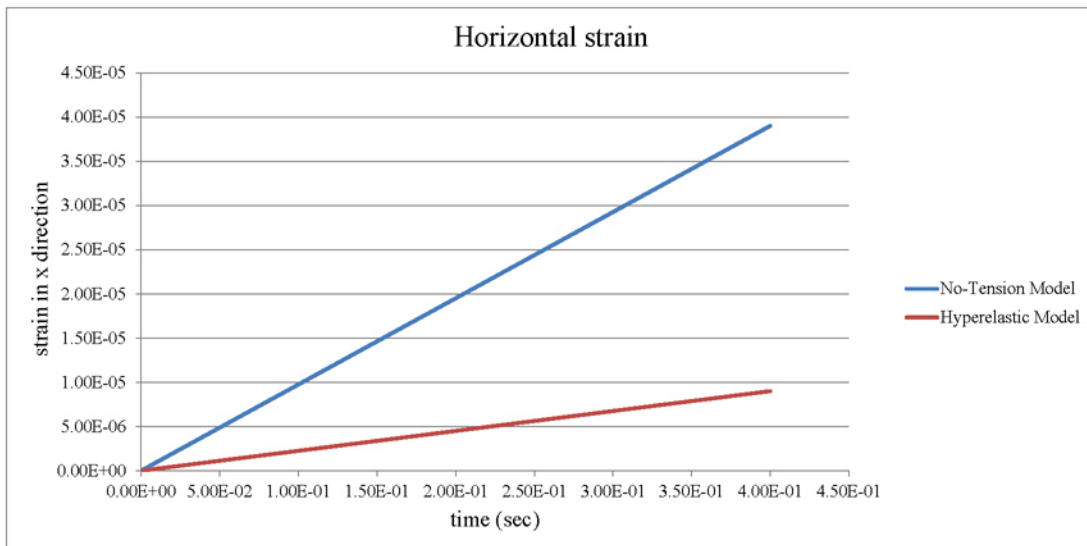


Figure 3. Strains in X direction

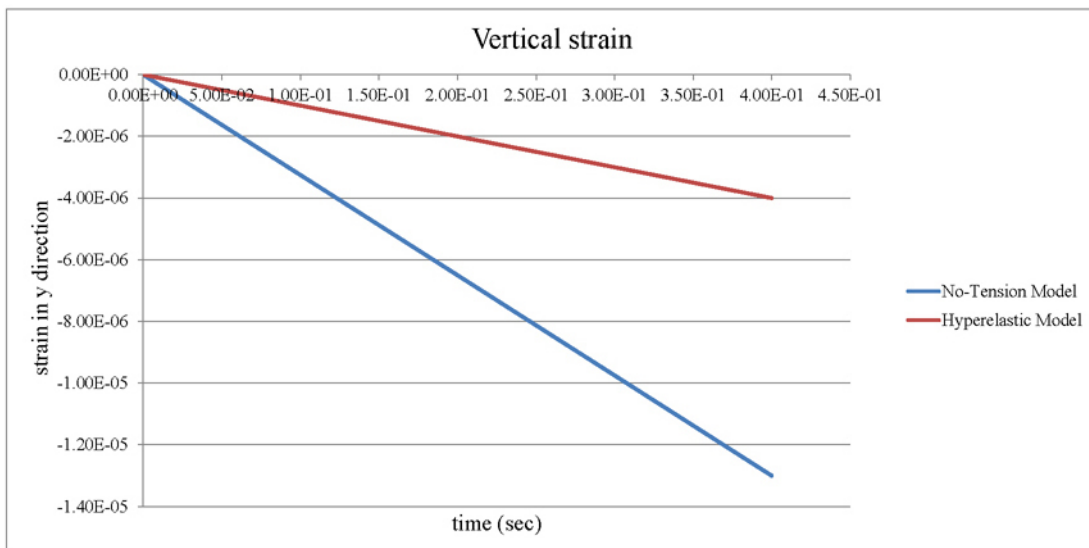


Figure 4. Strains in Y direction

Flexible pavement simulation

To understand the effect of granular base simulated as a no-tension material on pavement response, a two layer mesh was created and implemented into CAPA-3D. The material properties which were chosen are shown in Table I. Lamé's constants were calculated based on E and Poisson's ratio for the strain energy function and its derivatives. The Asphalt Concrete (AC) top layer with thickness of 150 mm was simulated as hyperelastic material while the base layer with a thickness of 1500 mm was specified in one case as a no-tension material and in another as hyperelastic.

Table I. Material Properties

Material Type	Model	E (MPa)	Poisson's ratio
AC layer	Hyperelastic Material	3500	0.35
Base	Hyperelastic Material	600	0.35
Base	No-tension Material	600	0.35

Boundary Condition

Due to symmetry of the geometry and load about the X-axis, half of the pavement was simulated. The model domain was chosen large enough to avoid any boundary effects. The structure was restrained at the bottom of the mesh to avoid movement along the X, Y and Z directions. Furthermore, it was restricted on the Y-Z and the Y-X planes to avoid movement along the X and the Z directions respectively, Figure 5(a).

Load Characteristics

Super single 495/45R22.5 tire loading was specified with a contact area of 428 mm and length of 180 mm [10] and a uniform pressure of 0.707 MPa. The distance between the center of two wheels was 1.887 m, Figure 5(a). In addition, gravity load was applied. The density for AC was specified as 2.39 gr/cm³ and for the base layer as 2.9 gr/cm³.

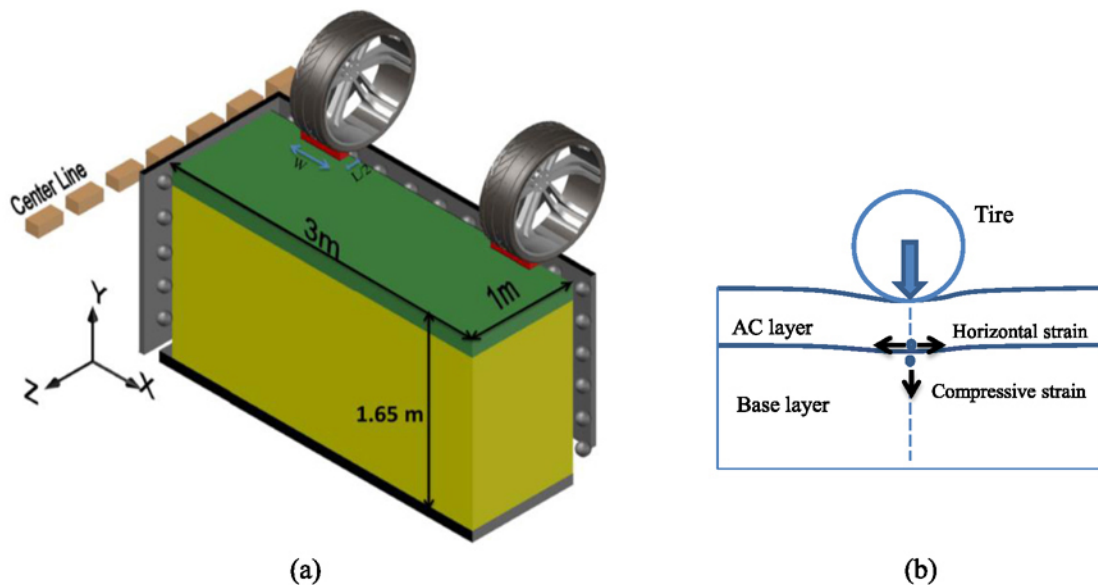


Figure 5. (a) FE pavement geometry and boundary conditions, (b) Critical locations for strain evaluation

Results of flexible pavement simulation

The effect of granular base material properties on the state of stress in the pavement, the vertical surface deflections and the strains at critical pavement locations, Figure 5(b), are now presented in the following.

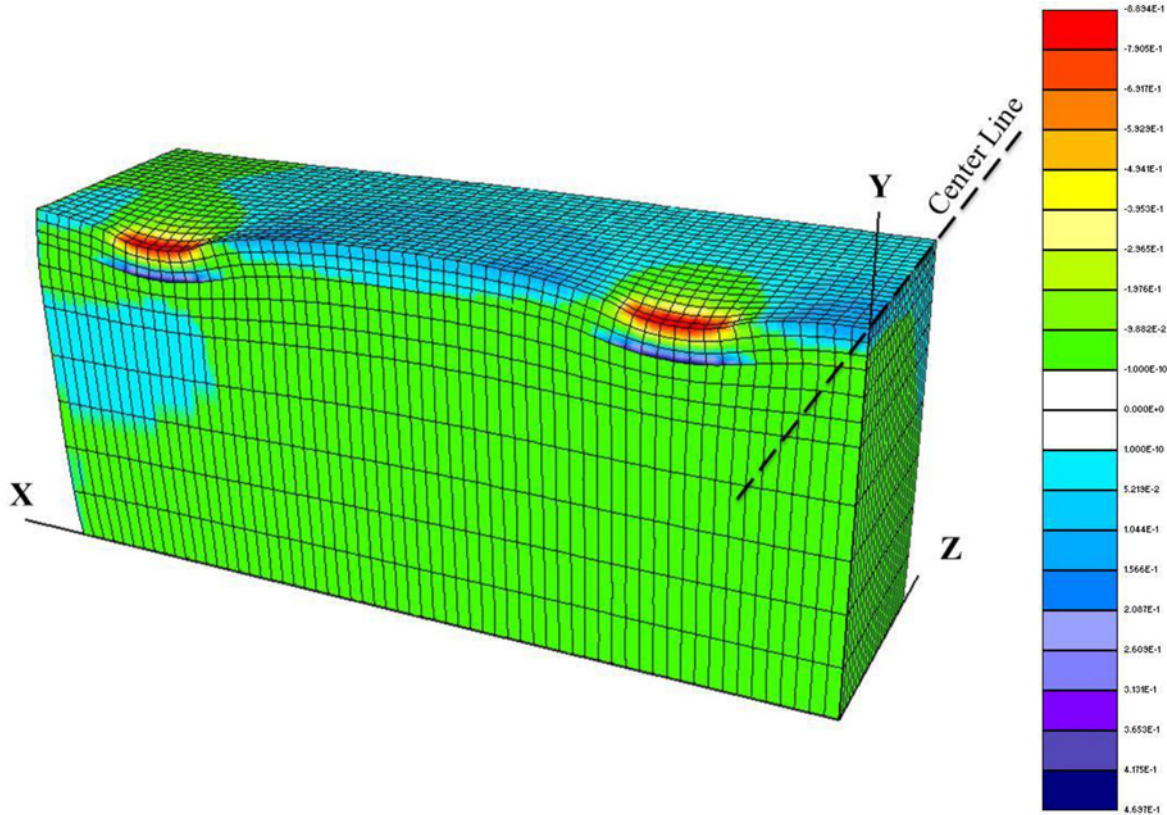


Figure 6. Stress distribution in the X direction in the pavement for hyperelastic base layer response

The three-dimensional state of stress over the height of the AC and base layer is plotted at the peak load in Figure 6 and 7. As it can be seen the pavement deforms more when the base layer is modeled by no-tension model.

Figure 8 shows the pavement surface vertical deflections for the two different base layer material models. As it is shown, when the material properties are specified as no-tension, the deflection of AC layer is almost 1.3 times higher than the case in which base layer was modeled by a hyperelastic model.

Also, from Figures 9 and 10 it can be concluded that tensile strains at the bottom of the AC layer and the vertical strains at top of the base layer are higher when the base layer is modeled by the no-tension model.

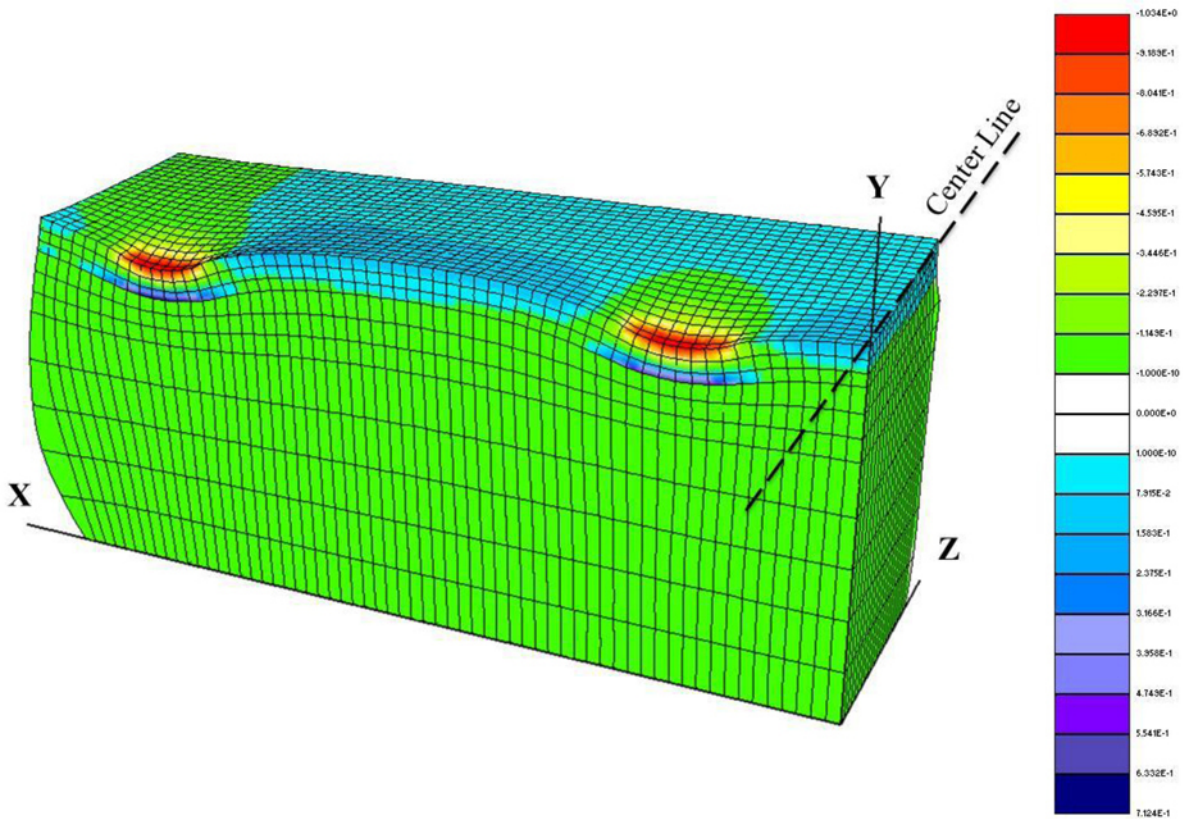


Figure 7. Stress distribution in the X direction in the pavement for no-tension base layer response

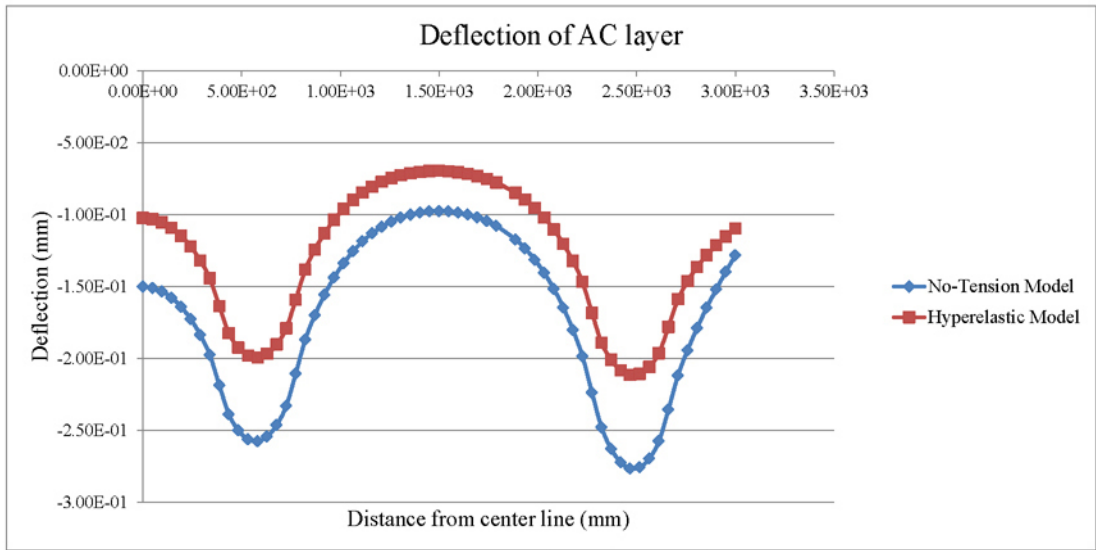


Figure 8. Deflection of AC layer along X axis

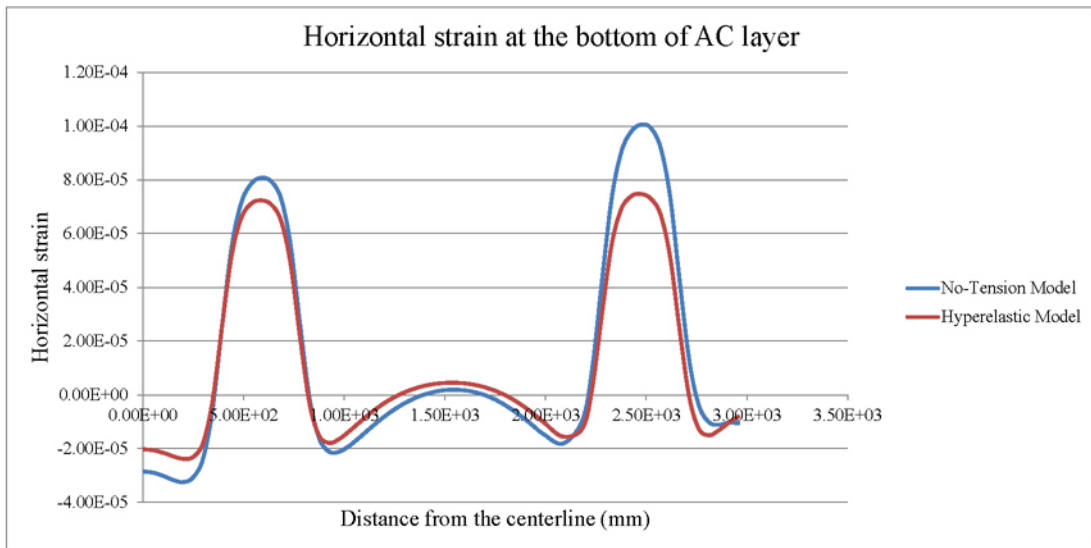


Figure 9. Horizontal strains at the bottom of AC layer for no-tension and hyperelastic model

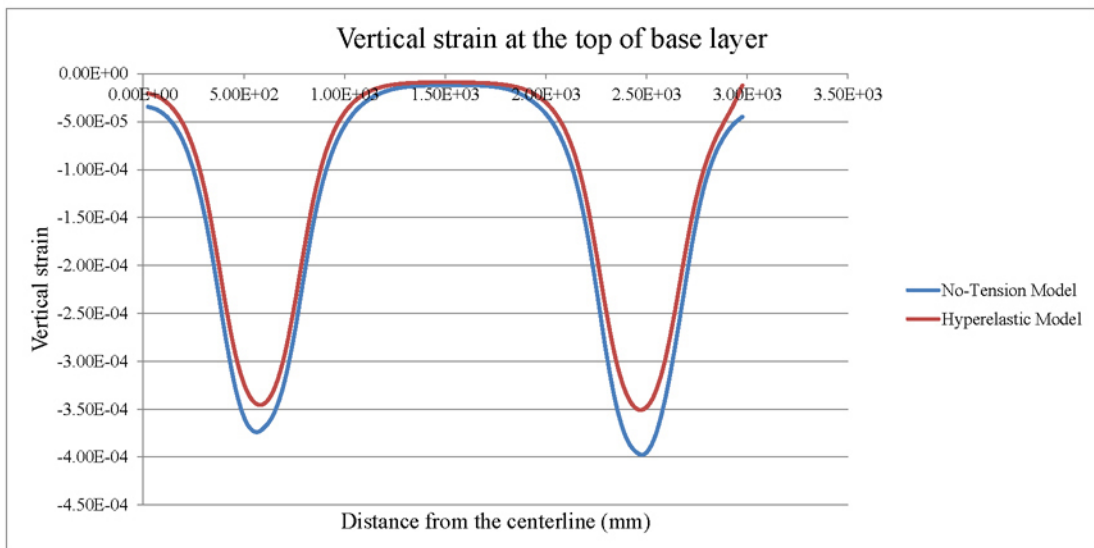


Figure 10. Vertical strains at the top of base layer for no-tension and hyperelastic model

Effect of No-Tension Model on State of Stress

In Figure 11, the distributions of compressive stresses at two different depths within the base layer along the horizontal axis are compared for the no-tension and the hyperelastic models in the presence of only one wheel. It can be seen that the compression stresses in the base layer have slightly higher values for the hyperelastic model compared to the no-tension model.

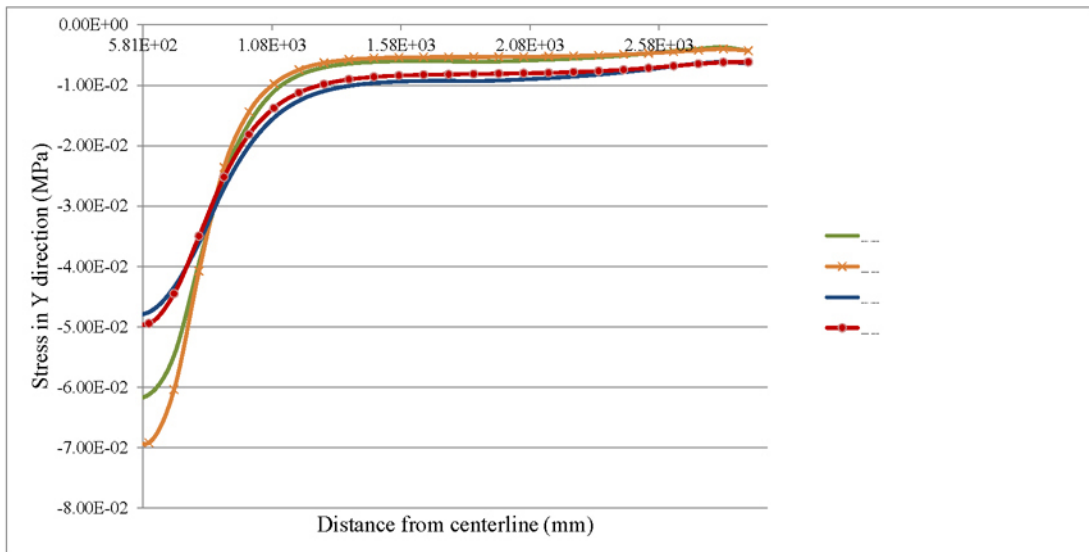


Figure 11. Base layer compressive stresses at Y=1450 mm and Y=1350 mm (see Figure 5(a)) of the base corresponding to the no-tension and hyperelastic material models for the granular base layer

Sensitivity analysis for no-tension model

A sensitivity analysis on the effect of Poisson's ratio on the pavement surface vertical deflection was carried out considering the base layer as a no-tension material. The results are plotted in Figure 12 and it can be seen that as Poisson's ratio increases, the vertical deflections of the pavement surface increase as well.

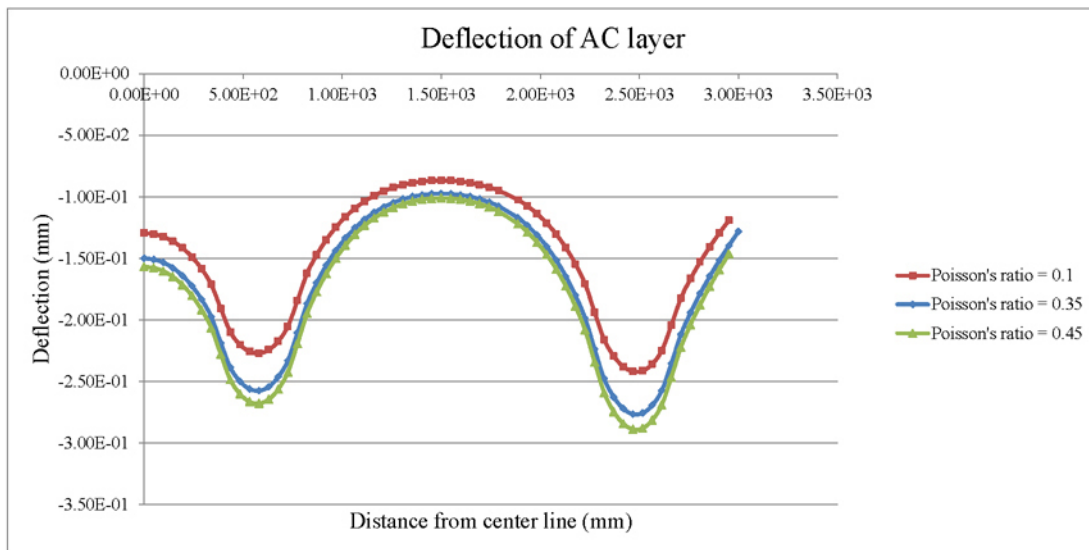


Figure 12. Top deflection of AC layer based on no-tension model for different values of Poisson's ratio

Conclusions

Evaluation of a no-tension constitutive model for simulation of the state of stress of granular materials utilized in pavement construction has indicated that significant differences in various pavement response parameters can be observed in comparison to typically utilized elastic models.

removal the capability of the granular material layer to resist tension has resulted to a significant increase in the overall flexibility of the pavement with corresponding consequences on the values of some of the typically utilized distress measures.

References

1. ARA, Inc., ERES Consultants Division, "Guide for Mechanistic–Empirical Design of New and Rehabilitated Pavement Structures" (Final report, NCHRP Project 1-37A, Transportation Research Board of the National Academies, 2004).
2. M. Kim, E. Tutumluer, and J. Kwon. "Nonlinear Pavement Foundation Modeling for Three-Dimensional Finite-Element Analysis of Flexible Pavements," *International Journal of Geomechanics*, 9 (5) (2009), 195-208.
3. S. Masad, D. Little, and E. Masad, "Analysis of Flexible Pavement Response and Performance Using Isotropic and Anisotropic Material Properties," *Journal of Transportation Engineering*, 132 (4) (2006), 342-349.
4. B. Saad, H. Mitri, and H. Poorooshab, "Three-Dimensional Dynamic Analysis of Flexible Conventional Pavement Foundation," *Journal of Transportation Engineering*, 131 (6) (2005), 460-469.
5. V. H. Nguyen, D. Duhamel, and B. Nedjar, "A Continuum Model for Granular Materials Taking Into Account the No-Tension Effect," *Mechanics of Materials*, 35 (2003), 955-967.
6. P. B. Lourenço, J. G. Rots, and J. Blaauwendraad, "Continuum model for Masonry: Parameter Estimation and Validation," *Journal of Structural Engineering*, 124 (6) (1998), 642-652.
7. Gerhard A. Holzapfel, *Nonlinear Solid Mechanics: A Continuum Approach for Engineering* (New York, NY: John Wiley & Sons, Inc., 2000).
8. A. Scarpas, "CAPA-3D: A mechanics based computational platform for pavement engineering" (PhD dissertation, Delft University of Technology, 2005).
9. J. C. Simo, and R. L. Taylor, "Quasi-incompressible Finite Elasticity in Principal Stretches. Continuum Basis and Numerical Algorithms," *Computer Methods in Applied Mechanics and Engineering*, 85 (1991), 273-310.
10. Effect of Wide Single Tyres and Dual Tyres. R.R. Addis. <http://www.minvenw.nl/rws/dww/home/cost334tyres/>. (2000).

INVESTIGATION AND MODELING OF THE FATIGUE DAMAGE IN NATURAL FIBER COMPOSITES

Habiba Bougherara¹, Ihab El Sawi¹, Zouheir Fawaz², Fodil Meraghni³

¹ Department of Mechanical and Industrial Engineering, Ryerson University, Toronto, ON, M5B2K3, Canada.

² Department of Aerospace Engineering, Ryerson University, Toronto, ON, M5B2K3, Canada.

³ LEM3 – UMRCNRS 7239, ARTS ET METIERS ParisTech, Centre de METZ, France

Keywords: Thermodynamic-based damage model, Natural fiber composites, Damage evolution.

Abstract

The main objective of this preliminary investigation is to identify and characterize the damage evolution of angle ply ($[\pm 45]_{16}$) flax-reinforced epoxy composites using an energy-based damage model combined with Scanning Electron Microscopy (SEM) observations. The damage model's parameters for the flax-reinforced epoxy composite were determined from quasi-static and fatigue tests. The preliminary results showed that the energy-based damage model is able predict accurately the damage rate in both longitudinal and transverse directions for loads. The mechanism of damage initiation in the flax/epoxy composites and the damage evolution, during each test, were monitored using SEM. A direct correlation between the microstructure of the flax-reinforced epoxy composites and the damage was obtained.

Introduction

Natural fibers such hemp, jute, and flax have attracted the attention of many researchers because of their potential to substitute synthetic fibers [1–4]. Since, the use of natural fiber composites in structural applications is fairly new, knowing the mechanical behavior of such materials, in particular, the fatigue life and damage accumulation is crucial in designing new natural fiber-based composite structures with high performances.

Unlike most engineering materials which exhibit a safe stress level called fatigue limit (or endurance limit) below which failure does not occur, fiber-reinforced polymer composites (FRPC) do not typically have such limit. Instead, they undergo a damage accumulation due to matrix cracking, delamination, interface fiber/matrix degradation, fiber breakage, etc. This damage accumulation phenomenon takes place during the entire material's life leading eventually to the progressive failure of the composite even at low applied stresses. The aim of this study is, therefore, to investigate and model the fatigue damage of flax fiber reinforced composites using thermodynamic-based damage model.

Materials and Methods

Flax/epoxy prepreg was purchased from LINEO, Belgium. The product type is a unidirectional (UD) flax fiber treated by a patented sizing and drying process (US Patent No. 8080288) and impregnated with partially cured epoxy resin system (Huntsman LY5150). The flax/epoxy prepreg has an area density of 180 g/m² with an epoxy content of 50 % per weight. Flax/epoxy laminate plates were manufactured using 16 layers of 300 mm X 300 mm sheets with ply [± 45]₁₆ orientation and. The material was placed on a plate in a sealed vacuum bagging set-up and cured in an autoclave at 150°C for 2h under 4 bar pressure while a 0.7 bar vacuum was maintained during the entire cure cycle. The tested specimens were 25 mm width, 250 length and 3 mm thickness.

Tension-tension fatigue tests were conducted on a servo-hydraulic MTS test machine equipped with a 100 kN load-cell capacity. Strain measurements were obtained using an extensometer with a 25 mm gage length, placed at the center of all specimens. Fatigue experiments were conducted in accordance with the ASTM standard D3479 at room temperature and under load control with a minimum to maximum stress ratio of 0.1 and a cyclic frequency of 5Hz. The fatigue limit was assumed to be reached for all tests that did not produce fatigue failure after 6 million cycles.

Fatigue damage model formulation

A fatigue damage model is developed through a phenomenological approach in the framework of thermodynamics. Based on the Ladevèze and Le Dantec work [1], the proposed model takes into account the damage stages characterizing the fatigue damage in natural fiber reinforced polymer matrix composites. Indeed, in such materials, the fatigue damage kinetic occurs according to three stages [2]: i) damage initiation corresponding to an important stiffness reduction during the early stage of damage evolution, namely the first thousands of cycles. ii) Coalescence and propagation of micro-cracks. This second stage is characterized by a behaviour accommodation and a relative steady damage evolution reduction. iii) Macroscopic cracks propagation, damage localization up to the final material failure. According to the continuum damage mechanics, the damage is introduced as an internal state variable coupled to elastic behaviour. The proposed damage model has been formulated through five damage variables [3-4] but in the present paper, only the formulation for in-plane damage involving three variables: d_{11} , d_{22} and d_{12} is considered. Assuming a thin structure (in-plane stress) where $s_{33}=0$, made of an orthotropic material, elastic moduli of the damaged material are then expressed as follows:

$$\begin{aligned} E_{11} &= E_{11}^0 (1 - d_{11}) \\ E_{22} &= E_{22}^0 (1 - d_{22}) \\ G_{12} &= G_{12}^0 (1 - d_{12}) \end{aligned} \quad (1)$$

E_{11} (resp. E_{22}) is the Young's modulus in the longitudinal (resp. transverse) direction. G_{12} is the in-plane shear modulus. d_{ij} are the damage variables associated to the corresponding moduli. The superscript 0 indicates initial values measured when $d_{ij}=0$.

For a damaged material, the elastic strain energy is dependent on the state variables d_{ij} . Then, the strain energy (W_d) of a damaged material is given by equation (2):

$$\begin{aligned}
W_d = & \frac{1}{2} \frac{1}{1-\nu_{12}\nu_{21}} \left[E_{11}^0 (1-d_{11}) \varepsilon_{11} \langle \varepsilon_{11} + \nu_{21} \varepsilon_{22} \rangle_+ + E_{11}^0 \varepsilon_{11} \langle \varepsilon_{11} + \nu_{21} \varepsilon_{22} \rangle_- \right] \\
& + \frac{1}{2} \frac{1}{1-\nu_{12}\nu_{21}} \left[E_{22}^0 (1-d_{22}) \varepsilon_{22} \langle \varepsilon_{22} + \nu_{12} \varepsilon_{11} \rangle_+ + E_{22}^0 \varepsilon_{22} \langle \varepsilon_{22} + \nu_{12} \varepsilon_{11} \rangle_- \right] + G_{12}^0 (1-d_{12}) \gamma_{12}^2
\end{aligned} \tag{2}$$

Where ($\langle A \rangle_+$) and ($\langle A \rangle_-$) stand for the positive and negative parts of A, respectively.

The damage affects E_{11} when $\varepsilon_{11} + \nu_{21} \varepsilon_{22}$ is positive and E_{22} when $\varepsilon_{22} + \nu_{12} \varepsilon_{11}$ is positive. For instance, when the composite is subjected to a longitudinal compressive loading, transverse cracks do not initiate damage and thus they don't have any effects on the damage evolution of the composite.

The dual thermodynamic variables Y_{ij} associated with the damage variables d_{ij} are deduced from the elastic strain energy W_d of the damaged material as follows:

$$\begin{aligned}
Y_{11} = & -\frac{\partial W_d}{\partial d_{11}} = \frac{1}{2} \left[\frac{1}{1-\nu_{12}\nu_{21}} E_{11}^0 \varepsilon_{11} \langle \varepsilon_{11} + \nu_{21} \varepsilon_{22} \rangle_+ \right] \\
Y_{22} = & -\frac{\partial W_d}{\partial d_{22}} = \frac{1}{2} \left[\frac{1}{1-\nu_{12}\nu_{21}} E_{22}^0 \varepsilon_{22} \langle \varepsilon_{22} + \nu_{12} \varepsilon_{11} \rangle_+ \right] \\
Y_{12} = & -\frac{\partial W_d}{\partial d_{12}} = \frac{1}{2} G_{12}^0 \gamma_{12}^2
\end{aligned} \tag{3}$$

In the present paper, the damage rate describing the damage kinetic with respect to the cycle number and is formulated as a sum of two components:

$$\dot{d}_{11} = \frac{\partial(d_{11})}{\partial(N)} = \frac{\alpha_{11} \beta_{11}}{1 + \beta_{11}} (Y_{11})^{\beta_{11}-1} + \lambda_{11} (Y_{11}) \left(e^{-(\delta_{11} N)} \right) \tag{4}$$

$$\dot{d}_{22} = \frac{\partial(d_{22})}{\partial(N)} = \frac{\alpha_{22} \beta_{22}}{1 + \beta_{22}} (Y_{22})^{\beta_{22}-1} + \lambda_{22} (Y_{22}) \left(e^{-(\delta_{22} N)} \right) \tag{5}$$

$$\dot{d}_{12} = \frac{\partial(d_{12})}{\partial(N)} = \frac{\alpha_{12} \beta_{12}}{1 + \beta_{12}} (Y_{12})^{\beta_{12}-1} + \lambda_{12} (Y_{12}) \left(e^{-(\delta_{12} N)} \right) \tag{6}$$

The first contribution, scaled by $(Y_{ij})^{\beta_{ij}-1}$ in equations (4) to (6), is derived from the Norton power law that describes the dissipation potential. The second component is introduced to describe the rapid stiffness reduction occurring during the cyclic loading. The state variables $d_{ij}(N)$ are obtained by numerical integration of the damage rates, with the initial conditions $d_{ij}(N=0) = d_{ij}^{fs}$.

Where d_{ij}^{fs} stands for the initial damage induced during the first loading ramp prior to the cyclic loading. These initial values are function of the applied stress level.

The developed fatigue damage model requires 12 parameters to be identified namely, four parameters per damage variable. In this work, the model is developed for tension-tension fatigue loading and hence 4 parameters have to be identified.

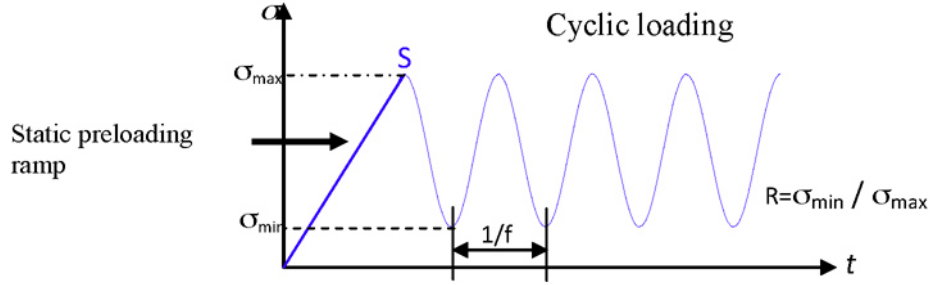


Fig. 1. Load history obtained from a force controlled fatigue test. Note that quasi-static preloading ramp (prior to the point S) gives rise to an initial damage representing the quasi-static damage (denoted by d_{qs}).

Model damage parameters identification procedure

An identification method involving homogeneous tensile fatigue tests have been used to determine the longitudinal damage parameters. The goal is to identify the parameters involved in the damage evolution, for the longitudinal direction (α_{11} , β_{11} , λ_{11} and δ_{11} governing the damage d_{11}). For this purpose, load control tension-tension fatigue tests on composite specimens have been performed in longitudinal direction [2]. These fatigue tests have been carried-out at three stress levels: $\sigma_{max} = 65\% \sigma_{UTS}$, $\sigma_{max} = 70\% \sigma_{UTS}$ and $\sigma_{max} = 80\% \sigma_{UTS}$. The applied stress ratio $R = \sigma_{min} / \sigma_{max}$ remains constant for the different configuration ($R = 0.1$) and the frequency was fixed up to 5Hz.

The identification procedure relies on a cost function $S(P)$ that has been built as an objective function representing, in the least squares sense, the difference between experimental and computed damage values. It has been minimized using the gradient-based Levenberg-Marquart (LM) algorithm [5-7] which can be written as follows:

$$S(\underline{P}) = \frac{\sum_{i=1}^a [d_i^{exp}(\underline{P}) - d_i^{num}]^2}{\sum_{i=1}^a (d_i^{exp})^2} \quad (7)$$

Where a is the number of experimental data. d_i^{exp} denotes the experimental damage values determined using the dynamic modulus reduction curve (**Fig. 3**): $d_i^{exp} = 1 - E_i(N) / E_0$. d_i^{num} are the computed damage values predicted by the developed model. \underline{P} is the unknown parameter vector that contains the model parameters (α_{11} , β_{11} , λ_{11} , δ_{11}).